energies

MDPI

Article

Thermal Loss Modelling and Sustainability-Oriented Optimisation of Glass Tube Solar Collectors

Robert Kowalik [1,*], Aleksandar Nešović [2] and Paweł Lesiak [1]

[1] Faculty of Environmental Engineering, Geodesy and Renewable Energy, Kielce University of Technology, Tysiaclecia P.P. 7, 25-314 Kielce, Poland; pawel_l_1991@wp.pl
[2] Institute for Information Technologies, University of Kragujevac, Liceja Kneževine, Srbije 1A, 34000 Kragujevac, Serbia; aca.nesovic@kg.ac.rs
* Correspondence: rkowalik@tu.kielce.pl

Abstract

Solar thermal collectors play an important role in low-temperature thermal systems, where reducing heat losses must be balanced against material demand, economic considerations, and environmental impacts. This study investigates the heat-loss and sustainability performance of glass tube solar collectors (GTCs) by jointly analysing heat-transfer mechanisms, structural complexity, and material-related environmental indicators. Four GTC configurations are examined: single-glazed collectors with air and vacuum insulation (SG + Air and SG + Vacuum) and double-glazed collectors with air and vacuum insulation (DG + Air and DG + Vacuum). An analytical equivalent thermal-network model based on iterative thermal-resistance calculations is developed to quantify coupled conductive, convective, and radiative heat losses through cylindrical glass envelopes over absorber temperatures of 40–90 °C and ambient temperatures of 10–30 °C. The thermal analysis is integrated with a unified multi-criteria decision-making framework employing hybrid AHP–Entropy weighting and the SAW and TOPSIS ranking methods. The decision model incorporates heat loss, embodied global warming potential, embodied energy, manufacturing and logistics cost proxies, material mass, and casing surface area. A simplified material-footprint assessment based on a consistent component-level inventory is additionally used to quantify material-related environmental burdens. The results demonstrate that vacuum insulation substantially reduces envelope heat losses compared with air-filled configurations by suppressing natural convection within the intermediate gap. The single-glazed configurations have a total material mass of 2.96 kg, a total embodied energy of 97.04 kWh, and an embodied GWP of 10.84 kg CO_2-eq, whereas the corresponding values for the double-glazed configurations are 5.60 kg, 165.15 kWh, and 14.27 kg CO_2-eq, respectively. Under the adopted baseline decision assumptions, the SG + Vacuum configuration provides the most favourable compromise between low heat loss, material demand, environmental burden, and economic criteria. The proposed framework provides a transparent basis for the comparative, sustainability-oriented assessment of glass tube solar collector designs by integrating physics-based heat-loss modelling with environmental indicators and multi-criteria decision support.

Keywords: glass tube solar collectors; thermal loss modelling; vacuum insulation; sustainability-oriented optimisation; low-temperature thermal systems; green energy technology

Academic Editor: Xiaohu Yang

Received: 21 July 2026
Revised: 4 September 2026
Accepted: 7 September 2026
Published: 22 September 2026

 https://doi.org/10.3390/en19194497

1. Introduction

Solar thermal systems play a significant role in low-carbon heating strategies for residential and industrial buildings, particularly in domestic hot water preparation and low-temperature space heating. Among these technologies, glass tube collectors (GTCs) offer strong thermal retention, especially when vacuum insulation is applied to suppress convective heat transfer. Despite notable advances in GTC design, the selection of an optimal configuration remains challenging, as thermal performance alone does not sufficiently capture the economic and environmental trade-offs that determine real-world deployment in building energy systems.

Considerable research efforts have focused on improving the thermal behaviour of GTCs through advanced absorber coatings [1–5], optical efficiency enhancements [6], and alternative collector geometries [7]. Vacuum tube systems have demonstrated superior insulation capabilities due to the absence of convective heat transfer between layers [8], while experimental studies have highlighted the influence of glass thickness, gap spacing, and material composition on thermal losses and operating temperature levels [9–11]. In parallel, analytical and numerical modelling approaches, including finite element and computational fluid dynamics simulations, have been widely applied to predict heat transfer mechanisms and support collector design optimisation [12,13]. However, most existing studies focus primarily on thermal performance metrics and address design parameters in isolation, without explicitly linking heat loss behaviour to broader sustainability and decision-oriented criteria relevant for building applications.

As solar thermal technologies move towards wider commercial adoption, collector design increasingly needs to be assessed from a holistic perspective that extends beyond heat retention alone. Material demand, manufacturing impacts, and life-cycle environmental performance play an important role in determining the overall suitability of solar collectors for building-integrated energy systems. Life Cycle Assessment (LCA) has proven effective in quantifying embodied energy and greenhouse gas emissions of solar technologies [14–16] and has been applied to flat-plate collectors [17–20], evacuated tube assemblies [21], and integrated solar water heating systems [22–24]. Nevertheless, comparative LCA studies that systematically evaluate multiple GTC configurations under identical operating conditions remain limited.

In parallel, Multi-Criteria Decision-Making (MCDM) methods have gained increasing attention as tools for supporting sustainable energy technology selection, enabling the simultaneous consideration of thermal, economic, and environmental indicators. Methods such as AHP, SAW, and TOPSIS have been successfully applied to evaluate performance trade-offs in renewable energy systems [25–29]. However, the integration of MCDM frameworks with physics-based heat loss modelling for glass tube solar collectors has received limited attention in the literature, particularly in the context of design-oriented decision support for building energy applications [30].

1.1. Research Gap

To date, no study has jointly compared single- and double-glazed GTCs with air and vacuum insulation layers under identical boundary conditions using an iterative thermal resistance model, while simultaneously incorporating geometric, economic, and environmental criteria. Furthermore, a unified framework combining thermal modelling, MCDM-based ranking, and life cycle environmental assessment for GTC optimization has not been demonstrated.

Accordingly, this study presents a comprehensive thermal and sustainability evaluation of four GTC configurations: single-glass with air insulation (SG + Air), single-glass with vacuum insulation (SG + Vacuum), double-glass with air insulation (DG + Air), and double-glass with vacuum insulation (DG + Vacuum). An iterative thermal resistance

https://doi.org/10.3390/en19194497

model is developed to account for conduction, convection, and radiation heat transfer across all layers, evaluated over absorber temperatures from 40 °C to 90 °C and ambient temperatures from 10 °C to 30 °C. In addition to thermal loss analysis, geometric (mass, casing area), economic (manufacturing and export cost), and environmental (embedded energy, CO_2 emissions) indicators are assessed. A Multi-Criteria Decision-Making process is applied using both SAW and TOPSIS methods, while a simplified cradle-to-grave LCA quantifies embodied energy and environmental footprint.

1.2. Novelty Statement

The main contribution of this study is the integration of iterative thermal loss modelling, multi-criteria sustainability evaluation, and Simplified Material-Footprint Assessment into a unified framework for the comparative selection of glass tube solar collector configurations.

The proposed iterative ETN framework enables the representation of non-linear radiative and convective heat transfer mechanisms while retaining the computational simplicity of resistance-based thermal modelling.

The proposed methodology provides a robust basis for evidence-based optimization of GTC systems, supporting material-efficient and low-emission solar thermal applications across diverse operating conditions.

A simplified material-footprint assessment was conducted to compare the material-related environmental burdens of the four GTC configurations. The assessment is limited to the explicitly quantified material inventory and does not constitute a complete ISO 14040/14044-compliant cradle-to-grave LCA [31,32]. Processes such as vacuum generation and sealing, coating deposition, detailed manufacturing energy, transportation, maintenance, replacements, disposal, and recycling credits are outside the quantitative system boundary.

2. Structural and Thermal Design of Glass Tube Collectors (GTCs)

This study considers four glass tube collector (GTC) configurations that differ in glazing structure and intermediate gap insulation. The variants result from combining either single-glazed (SG) or double-glazed (DG) envelope construction with either an air (AL) or vacuum (VL) interlayer. The four examined collectors, hereafter denoted as SG + AL, SG + VL, DG + AL, and DG + VL, represent a progressive increase in insulation performance and structural complexity. Front-sectional schematics are shown in Figure 1 (SGGTC in Figure 1a, DGGTC in Figure 1b).

The main construction parts of the SGGTC (Figure 1a) are the absorber (with dimensions of 100 × 1000 mm, Figure 2a) and a glass tube. The space between the absorber and the glass tube can be filled with air (AL) or vacuum (VL). The dimensions of the glass tube (interior diameter is 104 mm, exterior diameter is 110 mm) for SGGTC are shown in Figure 2b.

On the other side, another glass tube (interior diameter is 122 mm, exterior diameter is 128 mm; Figure 2c) participates in the DGGTC construction. Therefore, the DGGTC has two characteristic intermediate spaces: between the absorber and the interior glass tube (the first air or vacuum layer) and between the interior and exterior glass tube (the second air or vacuum layer). In the case of the DGGTC, the distance between the glass tubes is 6 mm.

To provide a clearer representation of the overall collector assembly and the spatial arrangement of its individual components, perspective cutaway views of the single- and double-glazed GTC configurations are presented in Figure 3. The three-dimensional schematics illustrate the relative positions of the absorber, integrated flow channel, glass envelope(s), and the corresponding air or vacuum insulation layers.

https://doi.org/10.3390/en19194497

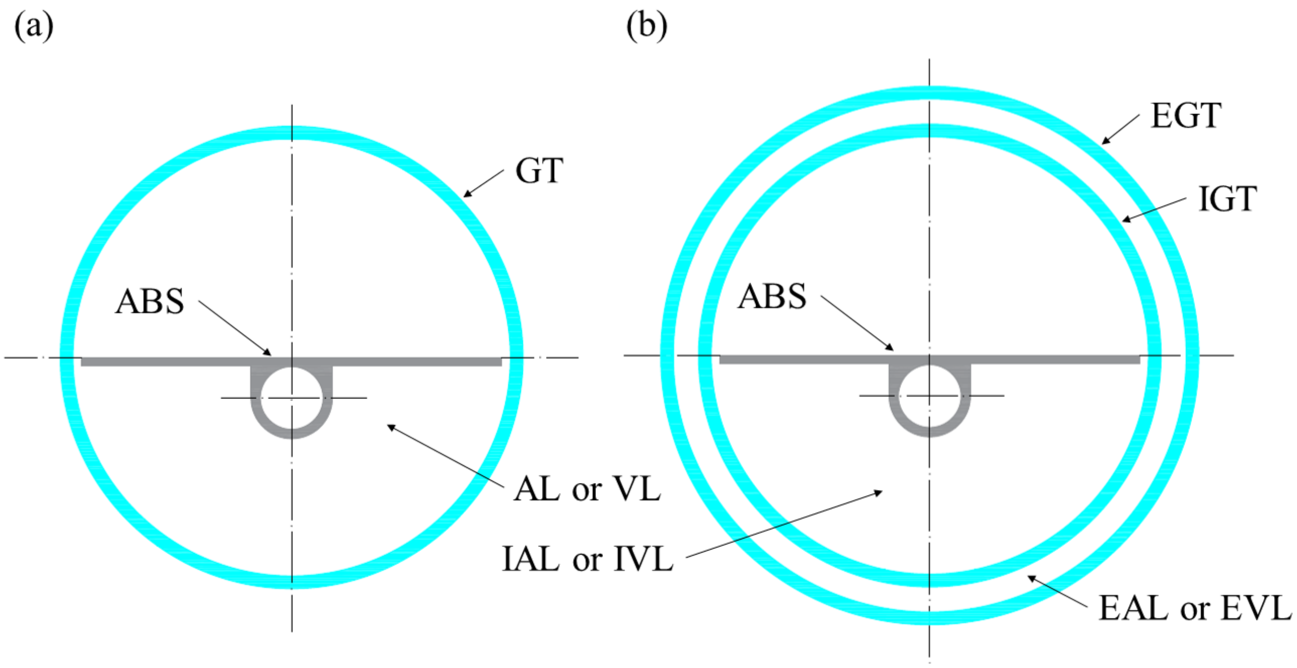

Figure 1. SGGTC (**a**) and DGGTC (**b**) in the transverse plane: ABS—absorber, GT—glass tube, AL—air layer, VL—vacuum layer, EGT—exterior glass tube, IGT—interior glass tube, IAL—interior air layer, EAL—exterior air layer, IVL—interior vacuum layer, EVL—exterior vacuum layer.

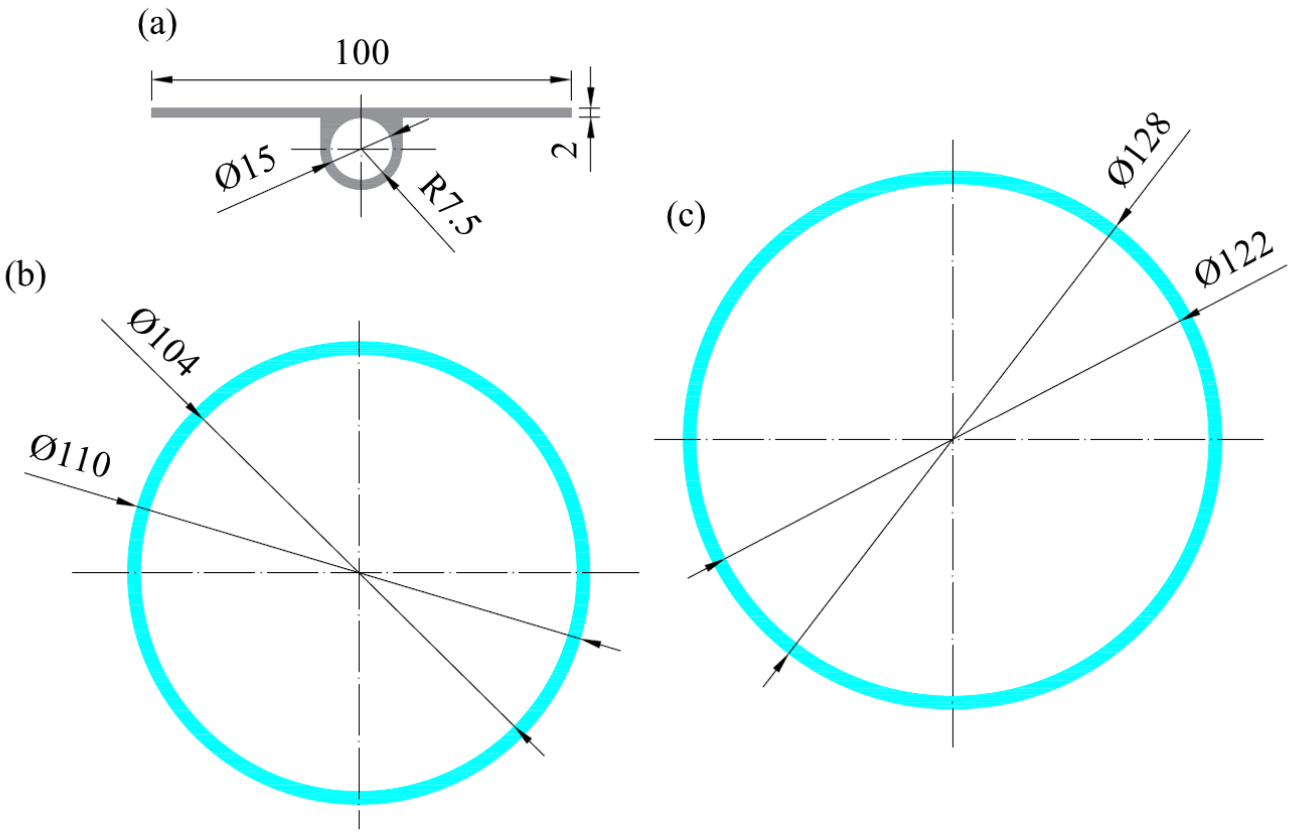

Figure 2. Dimensions of ABS (**a**), GT of the SGGTC and IGT of the DGGTC (**b**), and EGT (**c**) in the transverse plane.

In all four GTC configurations, the absorber includes an integrated circular flow channel with an internal diameter of 15 mm. This allows the circulation of water or working fluid, which can be driven either by gravity (natural circulation) or by a pump (forced circulation), depending on system integration. For simulation purposes, a nominal mass flow rate of 0.02–0.04 kg/s was considered, typical for residential solar thermal applications. The flow direction is assumed to be horizontal, aligned with the longitudinal axis of the absorber plate.

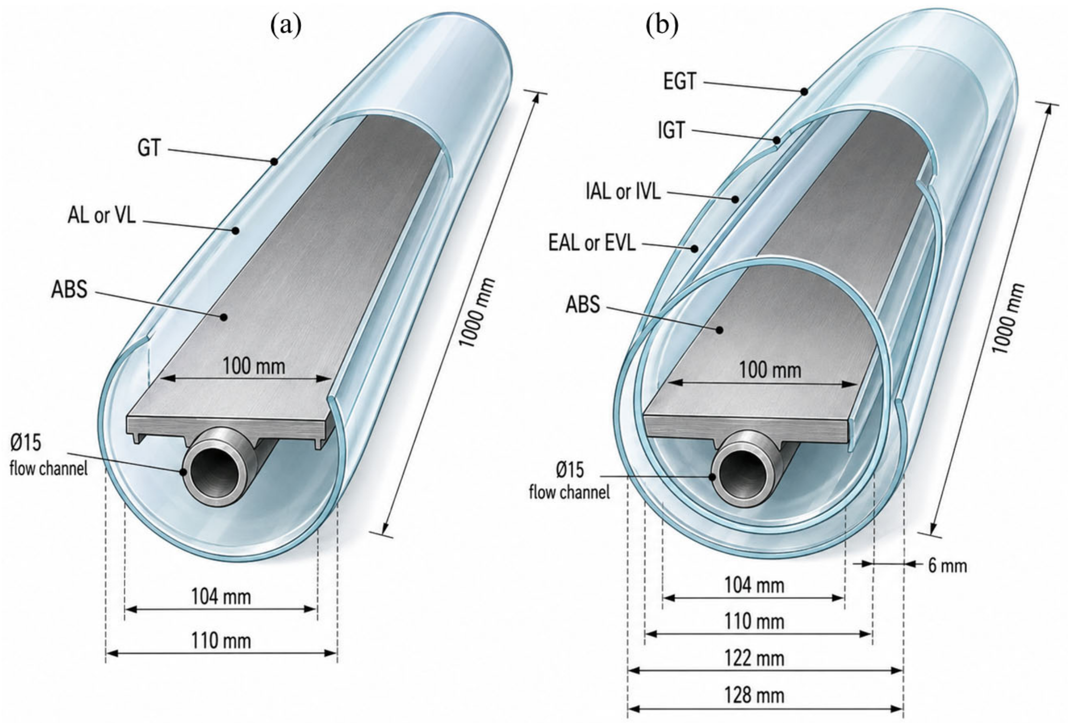

Figure 3. Perspective cutaway views of the analysed glass tube collector configurations: (**a**) single-glazed glass tube collector (SGGTC) and (**b**) double-glazed glass tube collector (DGGTC). ABS—absorber; GT—glass tube; IGT—interior glass tube; EGT—exterior glass tube; AL—air layer; VL—vacuum layer; IAL—interior air layer; IVL—interior vacuum layer; EAL—exterior air layer; EVL—exterior vacuum layer.

To summarize the differences between the four analyzed GTC configurations, Table 1 presents key design parameters.

Table 1. Comparative summary of geometric features of the GTC variants.

Parameter	SG + Air	SG + Vacuum	DG + Air	DG + Vacuum
Outer tube diameter [mm]	110	110	128	128
Glass thickness [mm]	3	3	3	3
Layer gap type	Air	Vacuum	Air–Air	Vacuum–Vacuum
Absorber width [mm]	100	100	100	100
Flow channel diameter [mm]	15	15	15	15
Total tube length [mm]	1000	1000	1000	1000

All systems are assumed to be mounted at a typical inclination angle of 35–45°, suitable for mid-latitude solar installations. The durability of the $SnAl_2O_3$ selective coating and the structural integrity of the vacuum layer were not explicitly analyzed in this study, but future work may focus on thermal fatigue and vacuum degradation under long-term exposure.

2.1. Geometric Configuration and Dimensional Parameters

The absorber is a flat aluminum plate with an integrated circular flow channel along its longitudinal axis. The fundamental geometry is provided in Figure 2 and summarized in Table 1. Dimensions were selected following standard residential-scale evacuated tube collectors and optimized for model comparability across configurations.

Key dimensions include:

Absorber width: 100 mm;

Total tube length: 1000 mm;

Internal hydraulic channel diameter: 15 mm;

Glass tube wall thickness: 3 mm;

SG internal/external diameters: 104/110 mm;

DG internal/external diameters: 122/128 mm;

Interlayer spacing in DG designs: 6 mm.

The geometric model assumes perfect cylindrical symmetry and negligible end losses relative to lateral heat transfer.

2.2. Material Properties and Optical–Thermal Characteristics

The absorber plate is made of aluminum coated with a $SnAl_2O_3$-based spectrally selective layer. This coating provides high solar absorptance and low thermal emittance (Table 2).

Table 2. Material properties and optical–thermal characteristics of the absorber and glass envelope used in all GTC configurations.

Property	Aluminum Absorber	Glass Tube(s)
Density ϱ [kg/m^3]	2700	2200
Specific heat c_p [J/(kg·K)]	900	660
Thermal conductivity k [W/(m·K)]	203	1.4
Thickness δ [mm]	2	3
Solar absorptance α [-]	0.95	–
Thermal emittance ε [-]	0.25	0.90

Material values were taken from validated sources and standardized datasheets used in solar thermal modeling literature.

2.3. Working Fluid and Hydraulic Operating Assumptions

All GTC types incorporate a single-pass internal flow channel designed for a water-based working fluid. The following assumptions apply:

- ✓ Working fluid: water, incompressible and Newtonian;
- ✓ Nominal mass flow rate: 0.02–0.04 kg/s;
- ✓ Flow direction: horizontal and parallel to the absorber plate;
- ✓ Flow regime: laminar to transitional (Re ≤ 3000);
- ✓ The internal convective heat-transfer coefficient is not explicitly included in the external heat-loss calculations.

The thermal modelling focuses exclusively on external heat losses, assuming that the internal convective resistance does not influence envelope-side heat transfer.

2.4. Installation and Boundary Conditions

The baseline calculations were performed using a fixed collector inclination angle of $\beta = 40°$. Ambient temperatures of 10, 20, and 30 °C and absorber temperatures from 40 to 90 °C in 10 °C increments were considered. A constant external wind speed of W = 1.0 m/s was adopted for all configurations.

Natural convection was considered only within the enclosed air-filled gaps and was evaluated using Rayleigh–Nusselt correlations. Convection within evacuated gaps was neglected. Heat transfer from the external glass surface to the ambient air was represented by the wind-dependent empirical correlation $h_{con,ext} = 2.8 + 3$ W, giving $h_{con} = 5.8$ W/(m^{2}K) for the adopted wind speed. No separate mixed-convection model was applied.

Thermophysical properties of air used in the Rayleigh, Prandtl, and Nusselt calculations were evaluated at the corresponding film temperature of each air gap.

3. Heat Losses Model of the GTCs

The thermal behaviour of glass tube collectors (GTCs) is governed by heat losses from the absorber to the ambient environment. In the considered configurations, these losses occur through three fundamental mechanisms:

1. Conduction through the solid materials (aluminum absorber and glass walls);
2. Convection within the enclosed gap for air-filled configurations;
3. Thermal radiation between surfaces at different temperatures.

In vacuum-based designs, the absence of a gaseous medium suppresses convection in the intermediate layer(s), so that radiative transfer becomes the dominant mechanism across the gap, while conduction is limited to the solid glass walls. No explicit vacuum pressure is prescribed; the evacuated gap is treated as an idealized limiting condition in which gaseous convection is suppressed. Residual-gas conduction and solid thermal bridges associated with seals or supports are neglected.

Although the proposed model is formulated using an Equivalent Thermal Network (ETN) approach, the overall system is non-linear. The non-linearity arises from temperature-dependent radiative heat transfer coefficients derived from the Stefan–Boltzmann law and from natural convection correlations based on Rayleigh–Nusselt relationships. Consequently, the thermal resistances are not constant but are iteratively updated during the calculation procedure until thermal equilibrium is reached.

The present ETN framework is specifically formulated to evaluate the external heat loss and insulation performance of the collector envelope under prescribed absorber and ambient temperatures. Solar optical gain, useful heat transfer to the working fluid, outlet-fluid temperature, and overall collector efficiency are not explicitly calculated. Consequently, the terms “thermal performance” used in the following analysis refer exclusively to heat-loss and thermal-insulation performance and should not be interpreted as complete solar-collector efficiency.

The dominant modes of heat transfer for air and vacuum configurations are summarized in Table 3. Air-filled gaps exhibit combined conductive and convective transport with moderate overall thermal resistance, whereas evacuated gaps eliminate convection and significantly increase the total resistance to heat loss.

Table 3. Dominant heat loss mechanisms for air and vacuum layers.

Heat Transfer Mechanism	Air Layer (AL)	Vacuum Layer (VL)
Conduction	Moderate (glass + air)	Minimal (glass only)
Convection	Significant	Negligible
Radiation	Present	Present
Total Resistance	Low	High

Boundary conditions used for the model assume fixed absorber temperatures (ranging from 40 °C to 90 °C) and ambient air temperatures (from 10 °C to 30 °C), as defined in the simulation framework. The internal water flow is assumed to have minimal effect on

https://doi.org/10.3390/en19194497

external heat loss due to the thermal isolation provided by the glass envelope and vacuum/air layer.

For vacuum-insulated configurations, convective heat transfer coefficients are eliminated from the thermal resistance model. This simplification allows the use of reduced Equation (1), such as:

$$R_{abs-gt} = \frac{1}{h_{rad,abs-gt} \cdot A_{gt}} \tag{1}$$

This form is used throughout Sections 3.1 and 3.2 for all vacuum-layer configurations.

A qualitative Thermal Network diagram (Figures 4 and 5) can be used to visualize these losses, where each layer (absorber, glass tube(s), and ambient air) acts as a thermal resistance element.

Heat losses Q_{loss} [W] of the SCs (applies also to the GTCs) can be described by Equation (2) [33]:

$$Q_{loss} = \frac{T_{abs} - T_o}{\sum R_{loss}} \tag{2}$$

where: T_{abs} [K] is the absorber temperature, T_o [K] is the ambient temperature, and ΣR_{loss} [K/W] is the resistance to heat transfer [34].

To facilitate comparison between different operating conditions and collector configurations, an overall heat-loss coefficient was additionally calculated as follows:

$$U_L = \frac{Q_{loss}}{A_{abs} \cdot (T_{abs} - T_o)} \tag{3}$$

In the present study, Aabs = 0.100 m^2 corresponds to the projected absorber area and is identical for all four configurations. The U_L coefficient therefore provides a normalized measure of envelope heat-loss performance independent of the imposed absorber-to-ambient temperature difference.

Resistance to heat transfer is equal to the sum of the resistance to heat transfer in the transverse plane $\Sigma R_{loss,\perp}$ [K/W] and the resistance to heat transfer in the longitudinal plane $\Sigma R_{loss,\parallel}$ [K/W], as shown in Equation (4) [34]:

$$\sum R_{loss} = \sum R_{loss,\perp} + \sum R_{loss,\parallel} \tag{4}$$

Since $\Sigma R_{loss,\parallel}$ [K/W] of the GTCs are negligibly small compared to $\Sigma R_{loss,\perp}$ (according to recommendations in [35]). A qualitative Thermal Network is shown in Figures 4 and 5, where each layer (absorber, glass tube(s), and ambient air) is represented as a series of thermal resistances. For the single-glazed GTC (SGGTC; absorber + one glass tube, Figures 1 and 4) and the double-glazed GTC (DGGTC; absorber + interior and exterior glass tubes, Figures 2 and 5), the transverse thermal resistance is written in Equation (5) [34] as a sum of the individual resistances between successive layers.

The model is developed under the following main assumptions:

- ✓ Steady-state conditions;
- ✓ One-dimensional radial heat transfer in the transverse plane;
- ✓ Negligible edge and longitudinal losses;
- ✓ Constant thermo-physical properties for each material at the reference temperature range;
- ✓ Diffuse-grey surfaces for radiative exchange;
- ✓ Natural convection in the air gaps, characterized by Rayleigh–Nusselt correlations.

These assumptions are standard in analytical models of evacuated and glass tube collectors and enable a balance between physical realism and computational tractability.

When the above is taken into account, ΣR_{loss} of the SGGTC (absorber plate and one glass tube, Figures 1 and 4) and the DGGTC (absorber plate, interior glass tube, and exterior glass tube, Figures 2 and 5) are given by Equation (5) [34]:

$$\sum R_{loss,\perp} \approx \begin{cases} SGGTC & R_{abs-gt} + R_{gt} + R_{gt-o} \\ DGGTC & R_{abs-gt,in} + R_{gt,in} + R_{gt,in-gt,ext} + R_{gt,ext} + R_{gt,ext-o} \end{cases} \quad (5)$$

where $R_{abs\text{-}gt}$ denotes the absorber–glass-tube thermal resistance, R_{gt} the glass-wall conduction resistance, and $R_{gt\text{-}o}$ the glass-tube–ambient resistance for the SGGTC. For the DGGTC, $R_{abs\text{-}gt,in}$, $R_{gt,in}$, $R_{gt,in\text{-}gt,ext}$, $R_{gt,ext}$, and $R_{gt,ext\text{-}o}$ denote, respectively, the absorber–inner-glass, inner-glass conduction, inner-to-outer-glass, outer-glass conduction, and outer-glass–ambient thermal resistances [K/W].

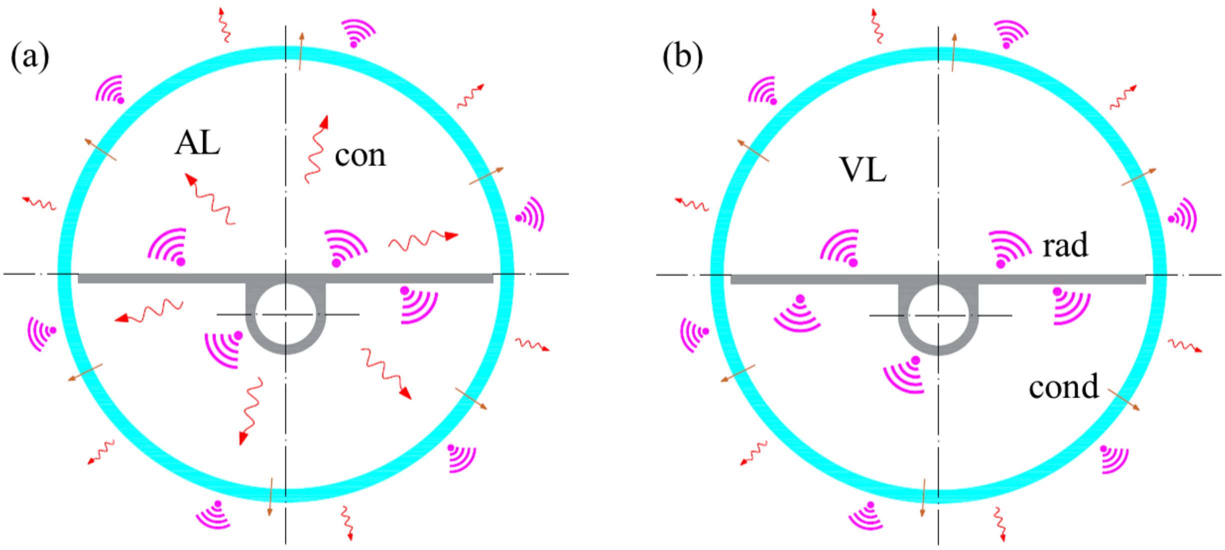

Figure 4. Heat energy transfer of the SGGTC with AL (**a**) or VL (**b**) in the transverse plane. Red wavy arrow line is con (convection), brown line is cond (conduction), purple Wi-Fi symbol is rad (radiation).

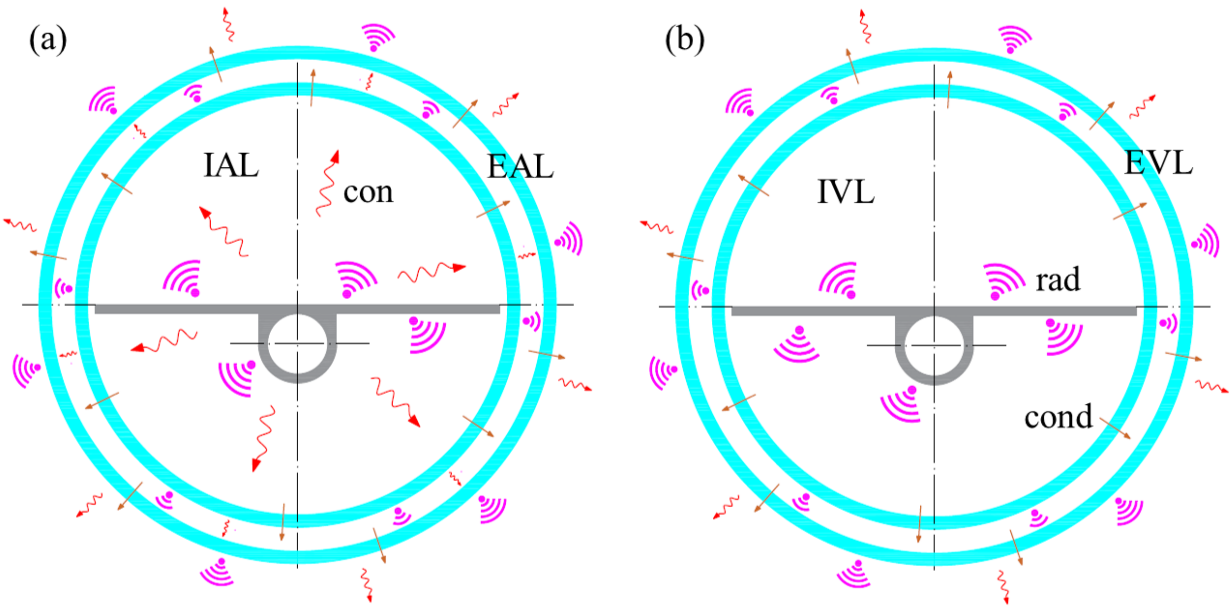

Figure 5. Heat energy transfer of the DGGTC with ALs (**a**) or VLs (**b**) in the transverse plane. Red wavy arrow line is con (convection), brown line is cond (conduction), purple Wi-Fi symbol is rad (radiation).

https://doi.org/10.3390/en19194497

3.1. Thermal Resistance Model of the SGGTCs

The single-glazed glass tube collector (SGGTC) consists of a flat absorber plate and a single glass tube (Figures 1a and 4). The intermediate space between the absorber (ABS) and the glass tube (GT) can be filled either with an air layer (AL) or with a vacuum layer (VL).

3.1.1. Thermal Resistance Formulation

When the ABS–GT gap is filled with air (SG + Air configuration), the total resistance between absorber and ambient is composed of:

- Combined radiative–convective resistance between absorber and glass tube;
- Conduction through the glass wall;
- Combined radiative–convective resistance between the outer glass surface and ambient air.

Formally, the absorber–glass resistance $R_{abs\text{-}gt}$ is a function of the radiative and convective heat transfer coefficients, as given in Equation (6) [34,36,37]:

$$R_{abs-gt} = \frac{1}{A_{abs,e,tot} \cdot \left(h_{rad(abs-gt)} + h_{con(abs-gt)}\right)} \tag{6}$$

where:

$A_{abs,e,tot}$ [m²] is the absorber total exterior area;

$h_{rad(abs\text{-}gt)}$ [W/(m²K)] is the absorber-glass tube radiation heat transfer coefficient;

$h_{con(abs\text{-}gt)}$ [W/(m²K)] is the absorber-glass tube convection heat transfer coefficient.

The radial conduction resistance through each homogeneous cylindrical glass wall was derived directly from Fourier's law in cylindrical coordinates. Accordingly, the logarithmic cylindrical resistance expression was used without an additional average-area correction factor. This avoids double counting of the cylindrical geometry and ensures that the resistance scales inversely with the collector length.

The glass conduction resistance and outer glass–ambient resistance are given by Equations (7) and (8), respectively. Together, these expressions define the total transverse thermal resistance of the SGGTC according to Equation (5).

Thermal resistances R_{gt} in Equation (7) and $R_{gt\text{-}o}$ in Equation (8) are (Figure 6) [34,36,37]:

$$R_{gt} = \frac{\ln\left(\frac{D_{gt,e}}{D_{gt,i}}\right)}{2 \cdot \pi \cdot k_{gt} \cdot L_{gt}} \tag{7}$$

$$R_{gt-o} = \frac{1}{A_{gt,e,tot} \cdot \left(h_{rad(gt-o)} + h_{con(gt-o)}\right)} \tag{8}$$

where:

$L_{gt} = L_{abs}$ [m] is the glass tube (absorber) length;

k_{gt} [W/(m·K)] is the glass tube thermal conductivity;

$D_{gt,e}$ [m] is the glass tube exterior diameter;

$D_{gt,i}$ [m] is the glass tube interior diameter;

$A_{gt,e,tot}$ [m²] is the glass tube total exterior area;

$h_{rad(gt\text{-}o)}$ [W(m²K)] is the glass tube–ambient air radiation heat transfer coefficient;

$h_{rad(gt\text{-}o)}$ [W/(m²K)] is the glass tube–ambient air convection heat transfer coefficient.

Heat transfer coefficients $h_{rad(abs\text{-}gt)}$ Equation (9), $h_{con(abs\text{-}gt)}$ Equation (10), $h_{rad(gt\text{-}o)}$ Equation (11), and $h_{con(gt\text{-}o)}$ Equation (12), respectively, are [36,37]:

$$h_{rad(abs-gt)} = \frac{\left(T_{abs}^2 + T_{gt}^2\right)\cdot\left(T_{abs} + T_{gt}\right)}{\frac{1}{\sigma\cdot\varepsilon_{abs}} + \frac{A_{abs,e,tot}}{A_{gt,i,tot}}\cdot\left(\frac{1}{\sigma\cdot\varepsilon_{gt}} - \frac{1}{\sigma}\right)} \tag{9}$$

$$h_{con(abs-gt)} = \frac{Nu_a \cdot k_a}{D_{gt,i,eq}} \tag{10}$$

$$h_{rad(gt-o)} = \sigma\cdot\varepsilon_{gt}\cdot\left(T_{gt}^2 + T_o^2\right)\cdot\left(T_{gt} + T_o\right) \tag{11}$$

$$h_{con(gt-o)} = 2.8 + 3\cdot W \tag{12}$$

where:

T_{gt} [K] is the glass tube temperature;
σ [W/(m^{2}K^4)] is the Stefan–Boltzmann constant;
ε_{abs} [-] is the absorber emissivity,
$A_{gt,i,tot}$ [m^2] is the glass tube total interior area;
ε_{gt} [-] is the glass tube emissivity,
Nu_a [-] is the Nusselt number of the air layer Equation (13) [38–41];
k_a [W/(m·K)] is the air layer thermal conductivity;
$D_{gt,i,eq}$ [m] is the air layer equivalent diameter;
W [m/s] is the wind speed.

In the present model, the external long-wave radiative exchange is represented using an equivalent-surroundings approximation. The sky, ground, and surrounding objects are not treated as separate radiative surfaces; instead, they are represented by a single effective radiative temperature assumed equal to the ambient air temperature, i.e., $T_{rad} = T_o$. Accordingly, Equation (11) corresponds to radiation exchange between the external glass surface and a large equivalent surrounding at T_o, with an effective view factor of unity.

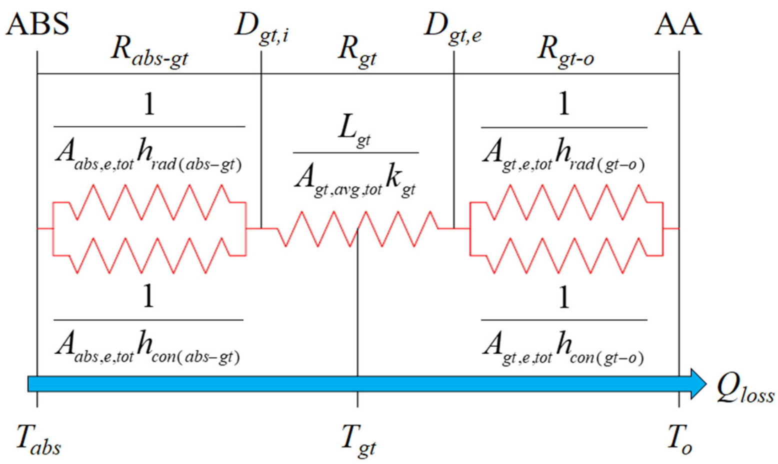

Figure 6. Heat transfer and thermal network of the SGGTC with AL (between ABS and GT).

The radiative and convective heat transfer coefficients used in Equations (6)–(8) are determined from Equations (9)–(12) [36,37]. Radiative exchange is expressed using the Stefan–Boltzmann constant σ [W/(m^{2}K^4)], surface emissivities ε_{abs} and ε_{gt}, and the relevant surface areas. Convective heat transfer inside the air gap is characterized via the Nusselt number as shown in Equation (13) [38–41]:

$$Nu_a = 1 + 1.44 \cdot \left\{ 1 - \frac{1708 \cdot \left[\sin\left(1.8 \cdot \beta_{gtc}\right) \right]^{1.6}}{Ra_a \cdot \cos \beta_{gtc}} \right\} \cdot \left[1 - \frac{1708}{Ra_a \cdot \cos \beta_{gtc}} \right]^{*} + \left\{ \left[\frac{Ra_a \cdot \cos \beta_{gtc}}{5830} \right]^{0.333} - 1 \right\}^{*} \quad (13)$$

where:

β_{gtc} [rad] is the inclined angle of the GTC;

Ra_a [-] is the Rayleigh number of the air layer in Equation (14) [38–41].

$$Ra_a = \frac{g \cdot \Pr_a \cdot \left(T_{abs} - T_{gt}\right) \cdot D^3_{gt,i,eq}}{T_a \cdot \nu_a^2} \quad (14)$$

where:

g [m/s^2] is the gravitational acceleration;

Pr_a [-] is the Prandtl numberof the air layer;

T_a [K] is the air layer temperature;

ν_a [m^2/s] is the air layer kinematic viscosity.

Characteristic areas and circumferences required for the resistance and coefficient formulations are introduced in Equations (15)–(18), while equivalent diameters and gap areas are derived in Equations (19) and (20).

The characteristic areas ($A_{abs,e,tot}$, $A_{gt,i,tot}$, $A_{gt,e,tot}$, and $A_{gt,avg,tot}$ are Equations (15)–(18):

$$A_{abs,e,tot} = O_{abs,e,\perp} \cdot L_{abs} \quad (15)$$

$$A_{gt,i,tot} = D_{gt,i} \cdot \pi \cdot L_{gt} \quad (16)$$

$$A_{gt,e,tot} = D_{gt,e} \cdot \pi \cdot L_{gt} \quad (17)$$

$$A_{gt,avg,tot} = \frac{A_{gt,i,tot} + A_{gt,e,tot}}{2} \quad (18)$$

where:

$O_{abs,e,\perp}$ [m] is the absorber circumference in the transverse plane;

L_{abs} [m] is the absorber length.

$D_{gt,i,eq}$ in Equations (10) and (14) is mathematically determined by Equation (19), while T_a is determined by Equation (20):

$$D_{gt,i,eq} = \frac{4 \cdot \left(A_{gt,i,\perp} - A_{abs,\perp}\right)}{O_{gt,i,\perp} + O_{abs,e,\perp}} \quad (19)$$

$$T_a = \frac{T_{abs} + T_{gt}}{2} \quad (20)$$

where:

$A_{gt,i,\perp}$ [m^2] is the glass tube interior area in the transverse plane;

$A_{abs,\perp}$ [m^2] is the absorber area in the transverse plane;

$O_{gt,i,\perp}$ [m^2] is the glass tube interior circumference in the transverse plane.

If the air layer is replaced by a vacuum layer, then Equation (6) eliminates the value $h_{con(abs-gt)}$.

3.1.2. Specific Assumptions for Air- and Vacuum-Filled Configurations

In the SG + Air configuration, heat is transferred from the absorber to the ambient through three successive resistances: absorber-to-glass radiation and convection, conduction through the glass tube, and external convection. In contrast, the SG + Vacuum model omits the convective term, simplifying the resistance chain and increasing total resistance.

For typical operating conditions (T_o = 20 °C, T_{abs} = 60 °C), the convective heat transfer coefficient h_{conv} between absorber and glass tube in SG + Air systems is approximately 2.5–5 W/(m²K), while radiative transfer coefficient h_{rad} ranges from 3 to 6 W/(m²K), depending on surface emissivity and view factor.

3.1.3. Dominant Mechanisms and Simplified Equations

On the basis of Equations (5)–(12), the total transverse thermal resistance of the single-glazed designs can be written in compact form as:

$$R_{SGTC+AL} = \frac{1}{(h_{con} + h_{rad}) \cdot A_{abs}} + \frac{t_{gl}}{k_{gl} \cdot A_{gl}} + \frac{1}{h_{ext} \cdot A_{gt}} \quad (21)$$

$$R_{SGTC+VL} = \frac{1}{h_{rad} \cdot A_{abs}} + \frac{t_{gl}}{k_{gl} \cdot A_{gl}} + \frac{1}{h_{ext} \cdot A_{gt}} \quad (22)$$

In SG + Air, both radiation and natural convection contribute to heat transfer in the ABS–GT gap. For typical operating conditions considered in this study (e.g., T_o = 20 °C, T_{abs} = 60 °C), the internal convective coefficient $h_{con(abs\text{-}gt)}$ is of the order of 2.5–5 W/(m²K), while the radiative coefficient $h_{rad(abs\text{-}gt)}$ ranges between 3 and 6 W/(m²K), depending on emissivities and view factors. Consequently, both mechanisms have comparable influence on the total resistance.

In SG + Vacuum designs, the absence of convection in the intermediate layer causes the radiative exchange to dominate the absorber–glass interaction. As a result, $R_{SGTC+AL}$ is substantially higher than $R_{SGTC+VL}$ directly translating into lower heat losses for the same boundary temperatures.

3.2. Thermal Resistance Model of the DGGTCs

In double-glass tube collectors (DGGTCs), the heat transfer pathway is longer and includes an additional intermediate glass wall, which increases the overall thermal resistance. The sequence of heat transfer is as follows: absorber → inner glass tube (IGT) → intermediate layer → external glass tube (EGT) → ambient.

The Thermal Network for the DGGTC with interior and exterior air layers (IAL and EAL) is shown in Figure 7. In this case (DG + Air), both gaps are filled with air, and heat is transferred by:

- Combined radiation and natural convection in the ABS–IGT gap;
- Conduction through the IGT wall;
- Combined radiation and natural convection in the IGT–EGT gap;
- Conduction through the EGT wall;
- Combined radiation and natural convection between the outer surface of the EGT and the ambient environment.

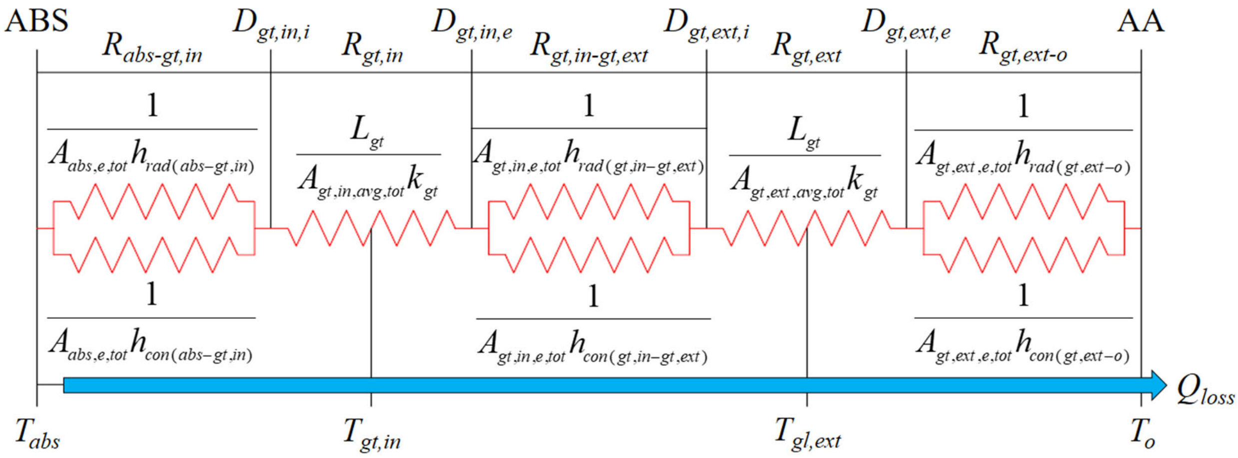

Figure 7. Heat transfer and thermal network of the DGGTC with IAL (between ABS and IGT) and EAL (between IGT and EGT).

The corresponding resistances are given in Equations (23)–(27) [34,36,37]. Radiative and convective heat transfer coefficients for the inner and outer gaps are defined in Equations (28)–(33), while the Rayleigh and Nusselt numbers for the interior and exterior air layers are obtained from Equations (34)–(37) [38–41]. Characteristic areas and circumferences associated with IGT and EGT are introduced in Equations (38)–(43), and auxiliary area terms are given in Equations (44) and (45).

Mathematical formulations of $R_{abs\text{-}gt,in}$ Equation (23), $R_{gt,in}$ Equation (24), $R_{gt,in\text{-}gt,ext}$ Equation (25), $R_{gt,ext}$ Equation (26), and $R_{gt,ext\text{-}o}$ Equation (27) are now shown (Figure 7) [34,36,37]:

$$R_{abs-gt,in} = \frac{1}{A_{abs,e,tot} \cdot \left(h_{rad(abs-gt,in)} + h_{con(abs-gt,in)}\right)} \tag{23}$$

$$R_{gt,in} = \frac{\ln\left(\frac{D_{gt,in,e}}{D_{gt,in,i}}\right)}{2 \cdot \pi \cdot k_{gt} \cdot L_{gt}} \tag{24}$$

$$R_{gt,in-gt,ext} = \frac{1}{A_{gt,in,e,tot} \cdot \left(h_{rad(gt,in-gt,ext)} + h_{con(gt,in-gt,ext)}\right)} \tag{25}$$

$$R_{gt,ext} = \frac{\ln\left(\frac{D_{gt,ext,e}}{D_{gt,ext,i}}\right)}{2 \cdot \pi \cdot k_{gt} \cdot L_{gt}} \tag{26}$$

$$R_{gt,ext-o} = \frac{1}{A_{gt,ext,e,tot} \cdot \left(h_{rad(gt,ext-o)} + h_{con(gt,ext-o)}\right)} \tag{27}$$

where:

$h_{rad(abs\text{-}gt,in)}$ [W/(m^{2}K)] is the absorber-interior glass tube radiation heat transfer coefficient;

$h_{con(abs\text{-}gt,in)}$ [W/(m^{2}K)] is the absorber-interior glass tube convection heat transfer coefficient;

$D_{gt,in,e}$ [m] is the exterior diameter of the interior glass tube;

$D_{gt,in,i}$ [m] is the interior diameter of the interior glass tube;

$A_{gt,in,e,tot}$ [m^2] is the exterior total area of the interior glass tube;

$h_{rad(gt,in-gt,ext)}$ [W/(m^{2}K)] is the interior glass tube-exterior glass tube radiation heat transfer coefficient,

$h_{con(gt,in-gt,ext)}$ [W/(m^{2}K)] is the interior glass tube-exterior glass tube convection heat transfer coefficient;

$D_{gt,ext,e}$ [m] is the exterior diameter of the exterior glass tube;

$D_{gt,ext,i}$ [m] is the interior diameter of the exterior glass tube;

$A_{gt,ext,e,tot}$ [m^2] is the exterior total area of the exterior glass tube;

$h_{rad(gt,ext-o)}$ [W/(m^{2}K)] is the exterior glass tube–ambient air radiation heat transfer coefficient;

$h_{con(gt,ext-o)}$ [W/(m^{2}K)] is the exterior glass tube–ambient air convection heat transfer coefficient.

In DG + Air configurations, both the absorber–IGT and IGT–EGT gaps are filled with air, which results in significant convective and radiative heat transfer. In DG + Vacuum configurations, both gaps are evacuated, eliminating convection and allowing only radiative transfer. This leads to a substantially higher overall thermal resistance in DG + Vacuum systems.

Table 4 summarizes the dominant heat transfer mechanisms for both double-glass configurations, providing a clear comparison between the air-filled and vacuum-insulated cases.

Table 4. Summary of dominant heat transfer modes in DGGTC configurations.

Layer	DG + Air	DG + Vacuum
Abs–IGT gap	Convection + Radiation	Radiation only
IGT–EGT gap	Convection + Radiation	Radiation only
Total resistance	Medium	Very high

As summarized in Table 4, DG + Air systems exhibit medium total resistance because both gaps provide radiative and convective paths for heat transfer. In DG + Vacuum systems, all intermediate heat transfer between the absorber and ambient (excluding conduction through glass) is radiative, leading to significantly higher resistance and reduced heat losses.

The coefficient $h_{rad(abs-gt,in)}$ can be described by Equation (28), $h_{con(abs-gt,in)}$ by Equation (29), $h_{rad(gt,in-gt,ext)}$ by Equation (30), $h_{con(gt,in-gt,ext)}$ by Equation (31), $h_{rad(gt,ext-o)}$ by Equation (32), and $h_{con(gt,ext-o)}$ by Equation (33) [36,37]:

$$h_{rad(abs-gt,in)} = \frac{\left(T_{abs}^2 + T_{gt,in}^2\right)\cdot\left(T_{abs} + T_{gt,in}\right)}{\frac{1}{\sigma\cdot\varepsilon_{abs}} + \frac{A_{abs,e,tot}}{A_{gt,in,i,tot}}\cdot\left(\frac{1}{\sigma\cdot\varepsilon_{gt}} - \frac{1}{\sigma}\right)} \tag{28}$$

$$h_{con(abs-gt,in)} = \frac{Nu_{a,in}\cdot k_{a,in}}{D_{gt,in,i,eq}} \tag{29}$$

$$h_{rad(gt,in-gt,ext)} = \frac{\left(T_{gt,in}^2 + T_{gt,ext}^2\right)\cdot\left(T_{gt,in} + T_{gt,ext}\right)}{\frac{1}{\sigma\cdot\varepsilon_{gt}} + \frac{A_{gt,in,e,tot}}{A_{gt,ext,i,tot}}\cdot\left(\frac{1}{\sigma\cdot\varepsilon_{gt}} - \frac{1}{\sigma}\right)} \tag{30}$$

$$h_{con(gt,in-gt,ext)} = \frac{Nu_{a,ext}\cdot k_{a,ext}}{D_{gt,ext,i,eq}} \tag{31}$$

$$h_{rad(gt,ext-o)} = \sigma \cdot \varepsilon_{gt} \cdot \left(T_{gt,ext}^2 + T_o^2\right) \cdot \left(T_{gt,ext} + T_o\right) \quad (32)$$

$$h_{con(gt,ext-o)} = 2.8 + 3 \cdot W \quad (33)$$

where:

$T_{gt,in}$ [K] is the interior glass tube temperature;

$A_{gt,in,u,tot}$ [m^2] is the interior total area of the interior glass tube;

$Nu_{a,in}$ [-] is the Nusselt number of the interior air layer Equation (34) [38–41];

$k_{a,in}$ [W/(m·K)] is the interior air layer thermal conductivity;

$D_{gt,in,i,eq}$ [m] is the interior air layer equivalent diameter;

$T_{gt,ext}$ [K] is the exterior glass tube temperature;

$Nu_{a,ext}$ [-] is the Nusselt number of the exterior air layer shown in Equation (35) [38–41];

$k_{a,ext}$ [W/(m·K)] is the exterior air layer thermal conductivity;

$D_{gt,ext,i,eq}$ [m] is the exterior air layer equivalent diameter.

$$Nu_{a,in} = 1 + 1.44 \cdot \left\{1 - \frac{1708 \cdot \left[\sin\left(1.8 \cdot \beta_{gtc}\right)\right]^{1.6}}{Ra_{a,in} \cdot \cos\beta_{gtc}}\right\} \cdot \left[1 - \frac{1708}{Ra_{a,in} \cdot \cos\beta_{gtc}}\right]^* + \left\{\left[\frac{Ra_{a,in} \cdot \cos\beta_{gtc}}{5830}\right]^{0.333} - 1\right\}^* \quad (34)$$

$$Nu_{a,ext} = 1 + 1.44 \cdot \left\{1 - \frac{1708 \cdot \left[\sin\left(1.8 \cdot \beta_{gtc}\right)\right]^{1.6}}{Ra_{a,ext} \cdot \cos\beta_{gtc}}\right\} \cdot \left[1 - \frac{1708}{Ra_{a,ext} \cdot \cos\beta_{gtc}}\right]^* + \left\{\left[\frac{Ra_{a,ext} \cdot \cos\beta_{gtc}}{5830}\right]^{0.333} - 1\right\} \quad (35)$$

where: $Ra_{a,in}$ [-] is the Rayleigh number of the interior air layer Equation (36) [38–41], and $Ra_{a,ext}$ [-] is the Rayleigh number of the exterior air layer Equation (37).

$$Ra_{a,in} = \frac{g \cdot \Pr_{a,in} \cdot \left(T_{abs} - T_{gt,in}\right) \cdot D_{gt,in,i,eq}^3}{T_{a,in} \cdot \nu_{a,in}^2} \quad (36)$$

$$Ra_{a,ext} = \frac{g \cdot \Pr_{a,ext} \cdot \left(T_{gt,in} - T_{gt,ext}\right) \cdot D_{gt,ext,i,eq}^3}{T_{a,ext} \cdot \nu_{a,ext}^2} \quad (37)$$

where:

$Pr_{a,in}$ [-] is the Prandtl number of the interior air layer;

$T_{a,in}$ [K] is the interior air layer temperature;

$\nu_{a,in}$ [m^2/s] is the interior air layer kinematic viscosity;

$Pr_{a,ext}$ [-] is the Prandtl number of the exterior air layer;

$T_{a,ext}$ [K] is the exterior air layer temperature;

$\nu_{a,ext}$ [m^2/s] is the exterior air layer kinematic viscosity.

Analogous Equations (17)–(20), characteristic areas are Equations (38)–(43):

$$A_{gt,in,i,tot} = D_{gt,in,i} \cdot \pi \cdot L_{gt} \quad (38)$$

$$A_{gt,in,e,tot} = D_{gt,in,e} \cdot \pi \cdot L_{gt} \quad (39)$$

$$A_{gt,in,avg,tot} = \frac{A_{gt,in,i,tot} + A_{gt,in,e,tot}}{2} \quad (40)$$

$$A_{gt,ext,i,tot} = D_{gt,ext,i} \cdot \pi \cdot L_{gt} \quad (41)$$

$$A_{gt,ext,e,tot} = D_{gt,ext,e} \cdot \pi \cdot L_{gt} \tag{42}$$

$$A_{gt,ext,avg,tot} = \frac{A_{gt,ext,i,tot} + A_{gt,ext,e,tot}}{2} \tag{43}$$

Values $D_{gt,in,i,eq}$ Equation (44) and $D_{gt,ext,i,eq}$ Equation (45) now are:

$$D_{gt,in,i,eq} = \frac{4 \cdot \left(A_{gt,in,i,\perp} - A_{abs,\perp}\right)}{O_{gt,in,i,\perp} + O_{abs,e,\perp}} \tag{44}$$

$$D_{gt,ext,i,eq} = \frac{4 \cdot \left(A_{gt,ext,i,\perp} - A_{gt,in,e,\perp}\right)}{O_{gt,ext,i,\perp} + O_{gt,in,e,\perp}} \tag{45}$$

where:

$A_{gt,in,i,\perp}$ [m^2] is the interior area of the interior glass tube in the transverse plane;

$O_{gt,in,i,\perp}$ [m^2] is the interior circumference of the interior glass tube in the transverse plane;

$A_{gt,ext,i,\perp}$ [m^2] is the interior area of the exterior glass tube in the transverse plane;

$O_{gt,ext,i,\perp}$ [m^2] is the interior circumference of the exterior glass tube in the transverse plane.

In the end, $T_{a,in}$ Equation (46) and $T_{a,ext}$ Equation (47) are:

$$T_{a,in} = \frac{T_{abs} + T_{gt,in}}{2} \tag{46}$$

$$T_{a,ext} = \frac{T_{gt,in} + T_{gt,ext}}{2} \tag{47}$$

If the air layer is replaced by a vacuum layer in the DGGTC construction, then Equation (23) eliminates the value $h_{con(abs\text{-}gt,in)}$, while Equation (25) eliminates the value $h_{con(gt,in\text{-}gt,ext)}$.

The total thermal resistance of DGGTCs can be expressed as follows. For DG + Air:

$$R_{DGTC+AL} = \sum_{i=1}^{2} \left(\frac{1}{\left(h_{con,i} + h_{rad,i}\right) \cdot A_i} \right) + \sum_{j=1}^{2} \left(\frac{t_j}{k_j \cdot A_j} \right) + \frac{1}{h_{ext} \cdot A_{egt}} \tag{48}$$

In DG + Air systems, the most dominant thermal resistance typically arises in the IGT–EGT interface due to its wider spacing and the combined convective and radiative mechanisms. In DG + Vacuum configurations, the heat transfer is governed entirely by radiation, with two sequential radiative barriers doubling the radiative resistance compared to SG + Vacuum.

3.3. Iterative Steady-State Solution Procedure

The coefficients involved in the Thermal Network depend nonlinearly on temperatures (especially radiative terms ∝ T^4) and on the Rayleigh–Nusselt relationships for natural convection. Therefore, the heat loss problem cannot be solved in closed form and requires an iterative numerical procedure to achieve thermodynamic equilibrium.

A dedicated iterative algorithm with:

- A double iteration loop for SGGTCs (Figure 8a);
- A triple iteration loop for DGGTCs (Figure 8b).

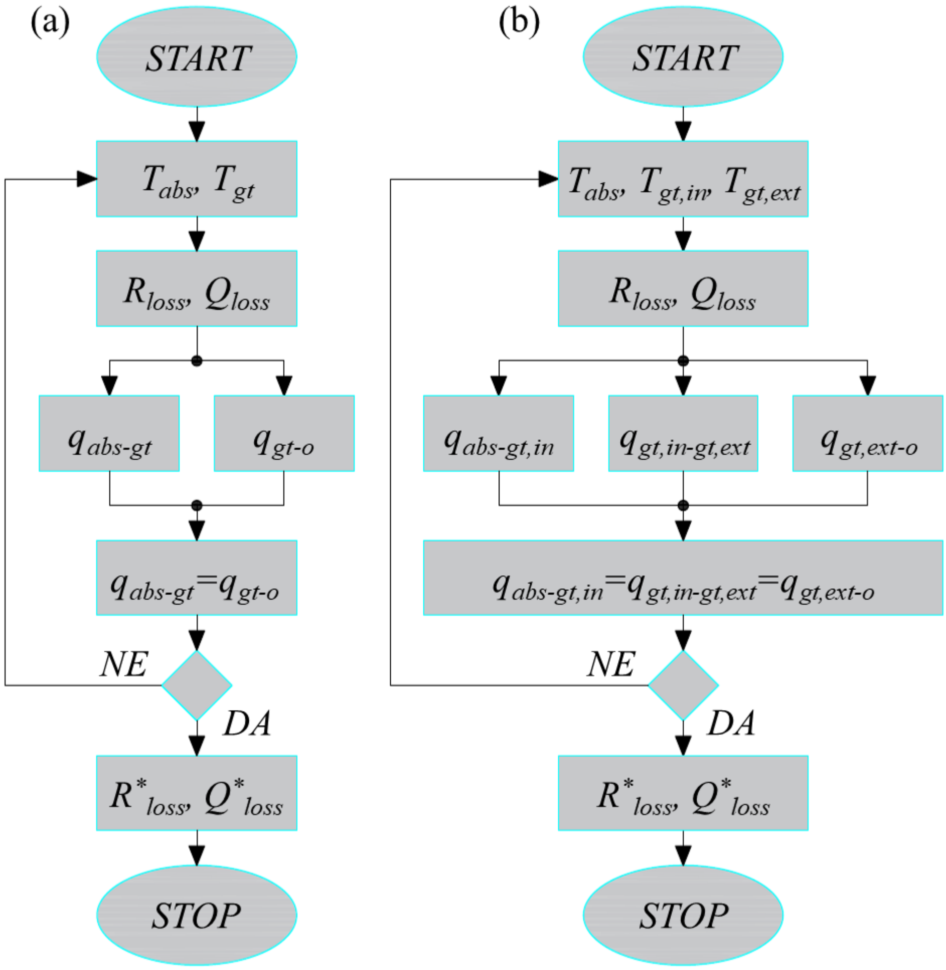

Figure 8. Iterative algorithm for the thermal loss calculation in single- (**a**) and double- (**b**) glass tube collectors.

Was implemented to solve for unknown temperatures at intermediate surfaces (glass tube(s) and air/vacuum layers) and the resulting heat loss.

The coefficients involved in the thermal network depend nonlinearly on temperature. In particular, radiative heat transfer coefficients are calculated from the Stefan–Boltzmann equation and therefore vary with surface temperatures. In addition, convective heat transfer coefficients are obtained from Rayleigh–Nusselt correlations, which depend on temperature differences within the collector. Consequently, thermal resistances are continuously updated during the iterative procedure, and the resulting ETN model exhibits nonlinear behaviour.

It should be emphasized that the present model is limited to steady-state conditions. The iterative procedure is used exclusively to determine thermal equilibrium temperatures and heat losses and does not represent a transient simulation. Therefore, thermal capacitances of the absorber, glass tubes, and working fluid are not included in the model.

A dedicated iterative algorithm was implemented to determine equilibrium temperatures and heat losses. Initial temperatures were assumed for all unknown surfaces, and the corresponding heat transfer coefficients and thermal resistances were calculated. The procedure was repeated until the difference between successive temperature estimates was below 0.01 °C. The resulting temperatures were subsequently verified using the heat flux balance Equations (50)–(55). The workflow of the algorithm is illustrated in Figure 8.

The mathematical model and iterative calculation procedures were implemented using Python 3.14.7 (Python Software Foundation) and MATLAB R2026a (MathWorks, Natick, MA, USA). Both computational environments were used to calculate the intermediate surface temperatures, temperature-dependent heat-transfer coefficients, thermal resistances, and heat losses for the investigated GTC configurations.

The resulting overall thermal resistances and heat loss values obtained from this model form the basis for the subsequent multi-criteria and life cycle assessments presented in Sections 4 and 5.

3.4. Model Validation

The predictive capability of the proposed Equivalent Thermal Network (ETN) model was quantitatively assessed using experimental data reported in a previous study on a single-glazed glass tube collector with an air layer [35]. In that study, the thermal-loss model was experimentally validated using data obtained during a four-month measurement campaign conducted from 15 July to 15 October 2021. The experimental boundary conditions, including ambient temperature and wind velocity, were matched with the corresponding conditions used in the analytical calculations.

Because no additional experimental campaign was performed within the scope of the present study, experimental values were digitized from the validation plots reported in [35] and subsequently compared with the predictions of the present ETN model. The SG + Air configuration was selected because its geometry and heat-transfer mechanisms correspond most closely to the experimentally tested collector configuration.

Figure 9 presents the comparison between the literature experimental data and the heat losses predicted by the present ETN model for ambient temperatures of 20 °C and 30 °C. The corresponding relative absolute errors are shown in Figure 9c.

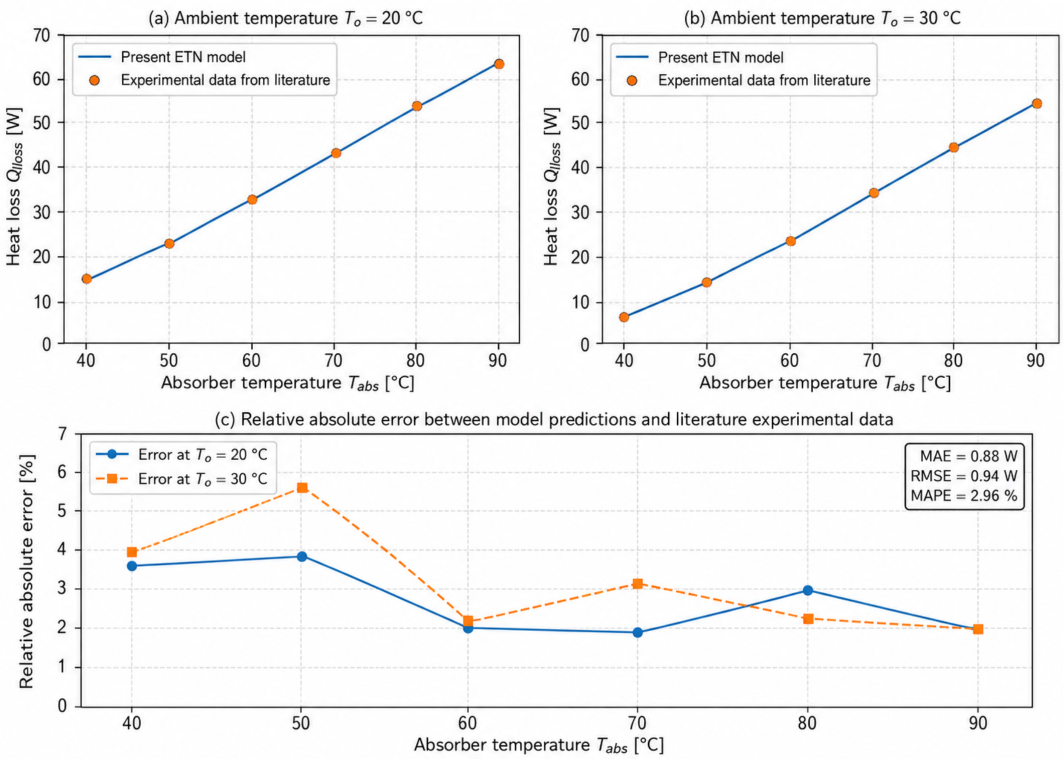

Figure 9. Validation of the developed ETN model against experimental data reported in the literature for the SG + Air configuration: (**a**) comparison of experimental and predicted heat losses at an ambient temperature of 20 °C; (**b**) comparison at an ambient temperature of 30 °C; (**c**) relative absolute error between the experimental and predicted values.

The comparison demonstrates close agreement between the experimental data and the ETN model predictions over the investigated operating range. Based on the digitized experimental values, the estimated mean absolute error (MAE) was 0.88 W, the root mean square error (RMSE) was 0.94 W, and the mean absolute percentage error (MAPE) was 2.96%. The maximum relative error was approximately 5.63%. A summary of the quantitative validation indicators is presented in Table 5.

Table 5. Quantitative validation of the present ETN model against experimental data reported in the literature.

Validation Indicator	Value
MAE [W]	0.88
RMSE [W]	0.94
MAPE [%]	2.96
Maximum relative error [%]	5.63
Validation configuration	SG + Air

The relatively small errors indicate that the simplified ETN formulation is capable of reproducing the experimentally observed heat-loss behaviour with satisfactory accuracy. The predicted heat losses also follow the experimentally observed increase with increasing absorber temperature. The error remained below approximately 6% throughout the analysed validation range, supporting the applicability of the model for steady-state thermal-loss calculations.

The physical trends predicted by the model are also consistent with other theoretical and experimental studies on glass tube and evacuated tube collectors. Previous investigations have demonstrated that vacuum insulation suppresses convective heat transfer within the collector envelope and consequently reduces thermal losses [33,35]. The present results reproduce this behaviour: vacuum-insulated configurations consistently exhibit higher overall thermal resistance and lower heat losses than their air-filled counterparts. In particular, the SG + Vacuum configuration reduced heat losses by up to 57.4% compared with SG + Air under identical boundary conditions.

Furthermore, the model reproduces the expected increase in heat losses with increasing absorber temperature and decreasing ambient temperature, consistent with behaviour widely reported for solar thermal collectors [1,33,35]. Although the present study does not include a new experimental campaign, the quantitative agreement with published experimental measurements, together with the consistency of the predicted physical trends with previous studies, provides confidence in the reliability of the proposed ETN model for steady-state analysis of glass tube solar collectors.

Quantitative validation was performed only for the SG + Air configuration, because this configuration most closely corresponds to the experimentally tested collector reported in Ref. [35].

4. Multi-Criteria Decision-Making (MCDM) Framework

The selection of an optimal glass tube collector (GTC) configuration requires a structured decision-making framework capable of incorporating multiple thermal, material, economic, and environmental criteria. To address this, a Multi-Criteria Decision-Making (MCDM) model is developed based on hybrid weighting (AHP + Entropy) and final ranking using the Technique for Order Preference by Similarity to Ideal Solution (TOPSIS).

The decision set consists of four GTC configurations:

A_1: SG + Air;

A_2: SG + Vacuum;

A_3: DG + Air;

A_4: DG + Vacuum.

It is known that the thermal performance of the mentioned SCs depends on their construction characteristics. However, in addition to their thermal performance, various other indicators should be taken into account, such as geometrical, economic, and ecological ones. In some situations, these indicators can greatly reduce, or even nullify, the main parameters of SCs: heat losses, thermal power, and thermal efficiency. It has been noticed that the authors very often do not look at new solar designs from different angles, i.e., a multidisciplinary approach.

In this paper, multi-criteria analysis (MCA) is used to arrive at an optimal solar design. Geometric (mass, total surface occupation, volume occupation), economic (manufacturing and exploitation costs), and ecological (embodied energy and greenhouse gas emissions) indicators are taken into account through the so-called MCA algorithm, as shown in Figure 10.

The goal function (the best solution is the minimum value) should arrive at the best measure, taking into account all indicators from Figure 10. This paper proposes a multi-criteria decision-making method (MCDM) that uses the Simple Additive Weighting (SAW) [42]. This model takes into account decision-maker preferences in the determination of the weights of the criteria [43]. It is a relatively simple model, and it provides relevant and reliable results. For each proposed indicator, a SAW score S_i [-] is calculated as Equation (49) [44]:

$$S_i = \sum_{i=1}^{n} w_j \cdot x_{ij} \text{, for } i = 1, 2, \ldots NOP \tag{49}$$

where: w_j [%] is the weight of j criterion performance, x_{ij} [-] is the normalized value of *i* in terms of *j* criterion, and *NOP* [-] is the number of proposed indicators.

The values of weight factors w_j are determined by their importance (their sum should be 100%).

Figure 10 and Table 6 show the main geometric indicators of ABS, GT (IGT), and EGT, and all of the GTC constructions.

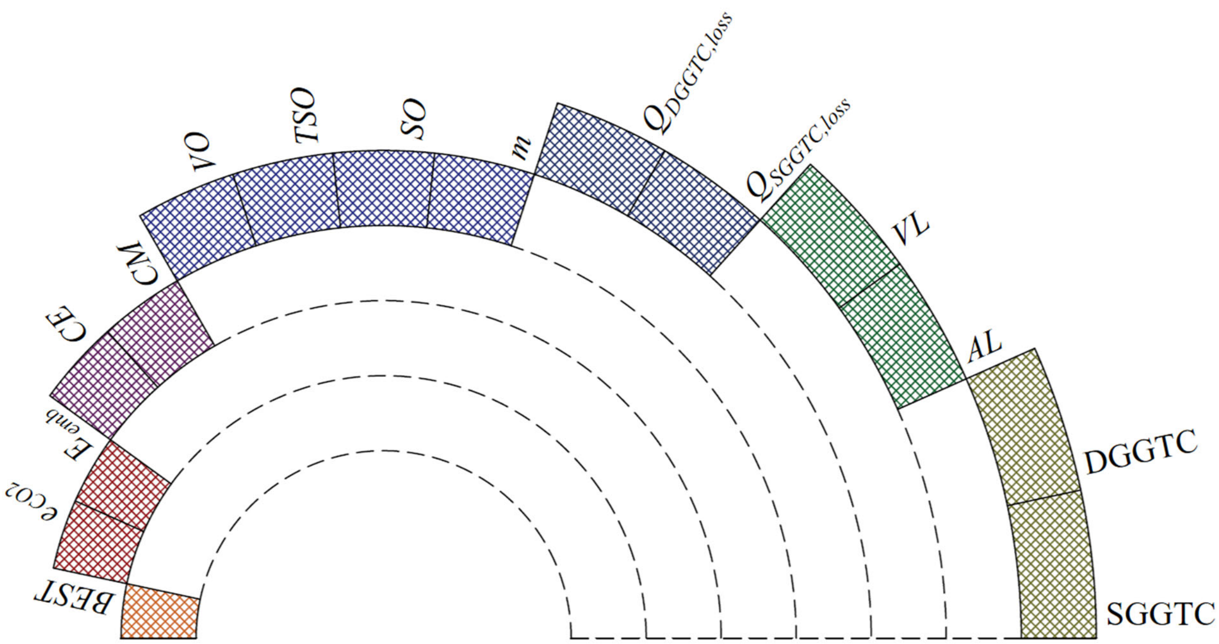

Figure 10. MCA algorithm for different GTCs: *m*—mass, *SO*—surface occupation, *TSO*—total surface occupation, *VO*—volume occupation, *CM*—manufacturing cost, *CE*—exploitation cost, E_{emb}—Embodied energy, e_{CO2}—CO_2 emission.

Table 6. Geometric indicators of the main components in the different GTC constructions.

Element	Material	ρ_{spec} [kg/m³]	m_{spec} [kg]	V_{spec} [m³]	SO_{spec} [m²]	TSO_{spec} [m²]	VO_{spec} [m³]
ABS	Aluminum	2700	0.76	0.00028	0.1	0.23	0.00047
GT *	Glass	2200	2.2	0.001	0.11	0.35	0.0095
EGT			2.64	0.0012	0.128	0.4	0.013

* GT in the SGGTC construction has the same dimension as IGT in the DGGTC construction.

The mass m [kg] of the SGGTC and the DGGTC can be determined as in Equation (50):

$$m \approx \begin{cases} SGGTC & m_{abs} + m_{gt} \\ DGGTC & m_{abs} + m_{gt,in} + m_{gt,ext} \end{cases} \tag{50}$$

where:

m_{abs} [kg] is the absorber mass of the SGGTC and the DGGTC;

m_{gt} [kg] is the glass tube mass of the SGGTC;

$m_{gt,in}$ [kg] is the interior glass tube mass of the DGGTC;

$m_{gt,ext}$ [kg] is the exterior glass tube mass of the DGGTC.

The SO [m²] Equation (51), TSO [m²] Equation (52), and VO [m³] Equation (53) of the SGGTC and the DGGTC are:

$$SO \approx \begin{cases} SGGTC & D_{gt,e} = 110 \text{ mm} \\ DGGTC & D_{gt,ext,e} = 128 \text{ mm} \end{cases} \tag{51}$$

$$TSO \approx \begin{cases} SGGTC & A_{gt,e,tot} = 0.35 \text{ m}^2 \\ DGGTC & A_{gt,ext,e,tot} = 0.4 \text{ m}^2 \end{cases} \tag{52}$$

$$VO \approx \begin{cases} SGGTC & \dfrac{D_{gt,e}^2 \cdot \pi}{4} \cdot L_{gt} = 0.0095 \text{ m}^3 \\ DGGTC & \dfrac{D_{gt,ext,e}^2 \cdot \pi}{4} \cdot L_{gt} = 0.013 \text{ m}^3 \end{cases} \tag{53}$$

Indicator MC [€] (manufacturing costs) can be determined for all analyzed cases using Equation (54):

$$MC \approx \begin{cases} SGGTC & \begin{cases} \text{with AL} & CM_{abs} + CM_{gt} \\ \text{with VL} & CM_{abs} + CM_{gt} + CM_{vl} \end{cases} \\ DGGTC & \begin{cases} \text{with AL} & CM_{abs} + CM_{gt,in} + CM_{gt,ext} \\ \text{with VL} & CM_{abs} + CM_{gt,in} + CM_{gt,ext} + CM_{vl,in} + CM_{vl,ext} \end{cases} \end{cases} \tag{54}$$

where (Field investigations):

CM_{abs} [€] is the absorber manufacturing cost of the SGGTC and the DGGTC (adopted: CM_{abs} = 25 €);

CM_{gt} [€] is the glass tube manufacturing cost of the SGGTC (adopted: CM_{gt} = 76 €);

CM_{vl} [€] is the vacuum layer manufacturing cost of the SGGTC (adopted: $CM_{vl} = 0.1 \cdot \left(CM_{abs} + CM_{gt}\right)$);

$CM_{gt,in}$ [€] is the interior glass tube manufacturing cost of the DGGTC (adopted: $CM_{gt,in}$ = 76 €);

$CM_{gt,ext}$ [€] is the exterior glass tube manufacturing cost of the DGGTC (adopted: CM_{gt} = 91 €);

$CM_{vl,in}$ [€] is the interior vacuum layer manufacturing cost of the DGGTC;

$CM_{vl,ext}$ [€] is the exterior vacuum layer manufacturing cost of the DGGTC (adopted: $CM_{vl,in} + CM_{vl,ext} = 0.15 \cdot \left(CM_{abs} + CM_{gt,in} + CM_{gt,ext}\right)$).

The exploitation costs CE [€], in Equation (55), in all cases, following Equation (54), during the use period (20 years), can be estimated at 50% of the CM:

$$CE \approx 0.5 \cdot CM \tag{55}$$

For the mentioned period (20 years) of the analyzed GTCs, total embodied energy E_{emb} [kWh] is given by Equation (56):

$$E_{emb} \approx \begin{cases} SGGTC & \dfrac{E_{emb,abs} + E_{emb,gt}}{20} \\ DGGTC & \dfrac{E_{emb,abs} + E_{emb,gt,in} + E_{emb,gt,ext}}{20} \end{cases} \tag{56}$$

where:

$E_{emb,abs}$ [kWh] is the absorber embodied energy of the SGGTC and the DGGTC Equation (57);

$E_{emb,gt}$ [kWh] is the glass tube embodied energy of the SGGTC Equation (58);

$E_{emb,gt,in}$ [kWh] is the interior glass tube embodied energy of the DGGTC Equation (59);

$E_{emb,gt,ext}$ [kWh] is the exterior glass tube embodied energy of the DGGTC Equation (60).

$$E_{emb,abs} = m_{abs} \cdot E_{emb,abs,spec} \tag{57}$$

$$E_{emb,gt} = m_{gt} \cdot E_{emb,gt,spec} \tag{58}$$

$$E_{emb,gt,in} = m_{gt,in} \cdot E_{emb,gt,spec} \tag{59}$$

$$E_{emb,gt,ext} = m_{gt,ext} \cdot E_{emb,gt,spec} \tag{60}$$

where:

m_{abs} [kg] is the absorber mass of the SGGTC and the DGGTC;

$E_{emb,abs,spec}$ [kWh/kg] is the specific absorber embodied energy of the SGGTC and the DGGTC (for aluminum: $E_{emb,abs,spec}$ = 53 kWh/kg [45]);

m_{gt} [kg] is the glass tube mass of the SGGTC;

$E_{emb,gt,spec}$ [kWh/kg] is the specific glass tube embodied energy of the SGGTC and the DGGTC (for glass: $E_{emb,gt,spec}$ = 25.8 kWh/kg [46]);

$m_{gt,in}$ [kg] is the interior glass tube mass of the DGGTC;

$m_{gt,ext}$ [kg] is the exterior glass tube mass of the DGGTC.

If the heat losses of the different GTCs were compensated by the electricity investment (from the electricity boiler, for example), the ecological indicator (CO_2 emission e_{CO2} [kg]) can be presented as Equation (61):

$$e_{CO2} = e_{CO2,el,spec} \cdot K_{el} \cdot \frac{E_{loss} \cdot time}{1000 \cdot \eta_{el}} \tag{61}$$

where:

$e_{CO2,el,spec}$ [kg/kWh] is the specific CO_2 emission (for electricity: $e_{CO2,el,spec}$ = 0.53 kg/kWh [47]);

K_{el} [-] is the primary energy transformation coefficient (for electricity: K_{el} = 2.5 [47]);

time [h] is the working time for 20 years (adopted: 2500 h/year);

η_{el} [-] is the efficiency of the electrical equipment used (for the electric boiler: η_{el}=0.98).

4.1. Criteria Definition and Classification

The evaluation of the four GTC configurations requires a set of criteria that collectively reflect heat-loss and thermal-insulation performance, environmental burden, and economic feasibility. Based on previous studies on solar thermal systems, sustainability assessment frameworks, and expert judgement in solar collector design, seven criteria were selected. These criteria capture both the operational behavior of the collectors (through thermal performance) and the life-cycle implications associated with material demand, manufacturing and transportation, and environmental impact.

The criteria are defined as follows (Table 7):

Table 7. Unified decision criteria used in both SAW and TOPSIS analyses.

Criterion	Raw Indicator	Orientation
C1	Q_{loss} [W]	Cost
C2	Embodied GWP [kg CO_2-eq]	Cost
C3	Embodied energy [kWh]	Cost
C4	Manufacturing cost [€]	Cost
C5	Transport/logistics cost [€]	Cost
C6	Mass [kg]	Cost
C7	Casing surface area [m^2]	Cost

4.1.1. Rationale for Criteria Selection

The selected criteria align with integrated sustainability assessment principles, in which system performance is defined not only by operational thermal advantages, but also by broader resource and environmental footprints. Notably:

- C1 represents the external heat-loss performance of the collector envelope under the common reference boundary conditions adopted for all alternatives. Lower Q_{loss} indicates better thermal-insulation performance.
- C2 and C3 represent environmental impacts consistent with Life Cycle Assessment (LCA), addressing climate change and energy depletion indicators.
- C4–C5 capture relevant economic considerations related to supply chain and production scalability.
- C6–C7 reflect material intensity and geometric implications that influence manufacturing feasibility, structural requirements, and transport logistics.

4.1.2. Benefit vs. Cost Orientation

Criteria are classified as benefit (higher values preferred) or cost (lower values preferred), as required for normalization and further multi-criteria processing. Formally:

$$B = \emptyset \qquad\qquad C = \{C2, C3, C4, C5, C6, C7\} \tag{62}$$

where B is the set of benefit criteria, and C is the set of cost criteria. All seven criteria are treated as cost criteria, for which lower values are preferred.

4.2. Subjective Weighting Using the Analytic Hierarchy Process (AHP)

The Analytic Hierarchy Process (AHP) is applied to derive subjective weights reflecting expert preferences on the relative importance of the evaluation criteria. AHP is a structured pairwise comparison method that translates qualitative assessments into quantitative priority values. It has been widely used in solar energy technology selection and multi-criteria sustainability assessments because it enables transparent justification of design priorities.

A pairwise comparison matrix A = [a_{ij}] is constructed using Saaty's 1–9 scale, where a_{ij} expresses how strongly criterion C_i is preferred to criterion C_j. For n = 7 criteria:

$$A = \begin{bmatrix} 1 & 2 & 2 & 3 & 4 & 6 & 9 \\ 1/2 & 1 & 1 & 2 & 3 & 5 & 8 \\ 1/2 & 1 & 1 & 2 & 2 & 4 & 7 \\ 1/3 & 1/2 & 1/2 & 1 & 2 & 3 & 5 \\ 1/4 & 1/3 & 1/2 & 1/2 & 1 & 2 & 4 \\ 1/6 & 1/5 & 1/4 & 1/3 & 1/2 & 1 & 2 \\ 1/9 & 1/8 & 1/7 & 1/5 & 1/4 & 1/2 & 1 \end{bmatrix} \quad (63)$$

The priority ordering adopted in this study—based on expert judgement and design practice in solar thermal systems—is:

$$C1 > C2 > C3 > C4 > C5 > C6 > C7 \quad (64)$$

Thus, heat loss Q_{loss} (C1) receives the highest subjective priority, followed by embodied GWP (C2), embodied energy (C3), manufacturing cost (C4), transport/logistics cost (C5), material mass (C6), and casing surface area (C7).

The normalized principal eigenvector of matrix A yields the AHP weight vector:

$$w^{AHP} = \{w_1^{AHP}, \dots, w_7^{AHP}\} \quad (65)$$

To verify the logical consistency of pairwise comparisons, the Consistency Ratio (CR) is calculated:

$$CR = \frac{CI}{RI}, CI = \frac{\lambda_{\max} - n}{n-1} \quad (66)$$

For the comparison matrix used in this study, λ_{max} = 7.0837, CI = 0.01395, and CR = 0.0106 < 0.10, indicating acceptable consistency according to Saaty's criterion.

The resulting AHP-derived weights are (Table 8):

Table 8. AHP-based subjective weights for the multi-criteria evaluation of GTC configurations, derived from expert pairwise comparisons (The calculated consistency ratio was CR = 0.073 (<0.10).

Criterion	**w^{AHP}**
C1—Heat loss Q_{loss}	0.328
C2—CO_2 emissions	0.210
C3—Embodied energy	0.188
C4—Manufacturing cost	0.121
C5—Export/transport cost	0.082
C6—Mass of materials	0.045
C7—Casing surface area	0.026

4.3. Objective Weighting Using the Entropy Method

The Entropy weighting method is applied to determine the objective contribution of each criterion based on the variability of performance values across the decision set. In contrast to AHP, which incorporates expert judgement, the Entropy method quantifies the information content of the data and assigns higher weight to criteria that exhibit greater discriminatory power. Thus, the technique mitigates subjectivity and enhances the robustness of the MCDM framework.

Let X = [x_{ij}] denote the decision matrix containing the performance values of the m = 4 m GTC alternatives (A1 = SG + Air, A2 = SG + Vacuum, A3 = DG + Air, A4 = DG + Vacuum) under $n = 7$ criteria (C1…C7).

To ensure comparability, the values are normalized following benefit/cost orientation:

For benefit criteria:

$$p_{ji} = \frac{x_{ji}}{\sum_{i=1}^{m} x_{ji}} \tag{67}$$

For cost criteria:

$$p_{ji} = \frac{\frac{1}{x_{ji}}}{\sum_{i=1}^{m} \frac{1}{x_{ji}}} \tag{68}$$

where p_{ij} is the normalized value of alternative A_i with respect to criterion C_j.

The entropy value of each criterion C_j is computed as:

$$e_j = -k \cdot \sum_{i=1}^{m} p_{ij} \cdot \ln(p_{ij}), k = \frac{1}{\ln(m)} \tag{69}$$

Given m = 4, we have $k = \frac{1}{\ln(4)}$.

Entropy e_j ranges from 0 (highest information content) to 1 (no discrimination capability).

Before computing objective weights, the degree of divergence is evaluated to measure the effective information contribution of each criterion. In the Entropy framework, criteria that exhibit greater variation across the evaluated alternatives provide more decision-relevant information, because they better discriminate among design options. Conversely, criteria with uniform values carry limited information and should receive lower importance.

Therefore, the divergence factor d_j is defined as the complement of the entropy value:

$$d_j = 1 - e_j \tag{70}$$

A larger d_j indicates stronger influence of criterion C_j on distinguishing between alternatives.

Once the divergence values are obtained, they are converted into the objective weight vector. The rationale is that criteria contributing more information (higher d_j) must receive higher importance in the decision model. To ensure normalization and comparability among all criteria, the divergence values are scaled as:

$$w_j^{ENT} = \frac{d_j}{\sum_{i=1}^{m} d_j} \tag{71}$$

This yields the entropy-based objective weighting vector:

$$w^{ENT} = \{w_1^{ENT}, w_2^{ENT}, \ldots, w_7^{ENT}\} \tag{72}$$

The resulting weights are free of subjective judgement and reflect the intrinsic structure of the performance data, thus complementing the AHP-derived expert preferences.

https://doi.org/10.3390/en19194497

4.4. Hybrid Weight Aggregation (AHP–Entropy)

A hybrid weighting strategy is employed to integrate both subjective knowledge of solar thermal system designers and the objective discriminatory power derived from the performance dataset. The rationale for hybrid weighting is that neither expert-based (AHP) nor data-driven (Entropy) weights alone can fully represent the multi-dimensional sustainability priorities associated with GTC development. Therefore, combining them improves the robustness and transparency of the evaluation.

To derive a unified weighting scheme, a convex combination of both vectors is applied:

$$w_j = \alpha \cdot w_j^{AHP} + (1-\alpha) \cdot w_j^{Entropy} \quad (73)$$

where:

$\alpha \in [0,1]$ is the hybridization coefficient that adjusts the relative strength of subjective vs. objective preference. A balanced approach is adopted in this study $\alpha = 0.5$ αMeaning that AHP- and Entropy-derived weights contribute equally to the final weight distribution. This value is consistent with recent applications of hybrid MCDM in solar energy system evaluation and ensures that:

- Expert-based design priorities (thermal resistance and emissions) are preserved;
- Data-driven variability across the decision set is adequately reflected.

The resulting hybrid weights are:

$$w = \{w_1, w_2, \ldots, w_3\} \quad (74)$$

summarized in Table 9.

Table 9. Final hybrid weights for the unified evaluation criteria (C1–C7), obtained using a 50:50 AHP–Entropy aggregation scheme.

Criterion	w_{AHP}	$w_{Entropy}$	w_j **Hybrid**
C1—Heat loss Q_{loss}	0.311	0.327	0.319
C2—Embodied GWP	0.224	0.020	0.122
C3—Embodied energy	0.173	0.010	0.092
C4—Manufacturing cost	0.128	0.267	0.197
C5—Transport/logistics cost	0.088	0.267	0.177
C6—Mass of materials	0.050	0.098	0.074
C7—Casing surface area	0.026	0.011	0.019
Sum	1.000	1.000	1.000

The revised hybrid weighting confirms that heat-loss performance (C1) remains the dominant criterion, with a final weight of 0.319. Manufacturing and transport/logistics costs follow with weights of 0.197 and 0.177, respectively. Environmental, material, and geometric criteria contribute lower individual weights. The same hybrid weighting vector is subsequently applied without modification in both the SAW and TOPSIS analyses.

Sensitivity analysis was performed by varying the AHP–Entropy aggregation coefficient from $\alpha = 0$ (pure Entropy weighting) to $\alpha = 1$ (pure AHP weighting) in increments of 0.1. In addition, each baseline hybrid criterion weight was individually perturbed by ±10% and ±20%, followed by renormalization of the complete weighting vector. The SG + Vacuum configuration remained the highest-ranked alternative in both SAW and TOPSIS throughout the entire α range and under all investigated weight perturbations. The ordering of the lower-ranked alternatives exhibited limited changes, indicating that the selection of the preferred alternative is substantially more stable than the complete ranking sequence.

https://doi.org/10.3390/en19194497

4.5. TOPSIS Ranking Procedure

The Technique for Order Preference by Similarity to Ideal Solution (TOPSIS) is used to obtain the final ranking of GTC configurations based on the hybrid weight vector derived in Section 4.4. TOPSIS is selected because it enables simultaneous consideration of benefit and cost criteria and ranks alternatives according to their geometric closeness to the ideal solution. This makes it particularly suitable for energy system selection problems where trade-offs between performance and environmental–economic factors are present.

Let A1 = SG + Air, A2 = SG + Vacuum, A3 = DG + Air, A4 = DG + Vacuum, evaluated under criteria C1 …C7. The hybrid weight vector is [Equation (75)].

The decision matrix X = [x_{ij}], where i = 1, …, 4 j = 1, …, 7, is normalized using vector normalization:

$$r_{ij} = \frac{x_{ij}}{\sqrt{\sum_{i=1}^{m} x_{ij}^2}} \tag{75}$$

yielding the normalized matrix R = [r_{ij}].

The hybrid weights are applied as:

$$v_{ij} = w_j \cdot r_{ij} \tag{76}$$

producing the weighted normalized matrix V = [v_{ij}].

4.6. Comparison of SAW and TOPSIS Methods in MCDM

In addition to the Simple Additive Weighting (SAW) method used in the main analysis, the Technique for Order Preference by Similarity to Ideal Solution (TOPSIS) was also applied for validation and comparative purposes. TOPSIS is a well-established multi-criteria decision-making method, which ranks alternatives based on their relative closeness to the ideal and anti-ideal solutions.

Using the same set of normalized specific indicators from Table 7 and the same weighting factors from Table 9, a normalized decision matrix was created. Each criterion was then weighted, and the Euclidean distance of each alternative from the ideal (best) and anti-ideal (worst) solution was calculated. The final ranking was determined using the closeness coefficient, which represents the ratio between the distance to the anti-ideal and the sum of both distances.

$$C_i = \frac{S_i^-}{S_i^- + S_i^+} \tag{77}$$

where:

C_i is the closeness coefficient of alternative *I*;

S_i^- is the Euclidean distance to the anti-ideal solution;

S_i^+ is the Euclidean distance to the ideal solution.

The higher the value of C_i, the closer the alternative is to the ideal solution. The alternatives are ranked in descending order of C_i.

The ranking of the four collector types remained identical to that obtained by the SAW method, confirming the robustness of the selection model:

- ✓ SGGTC with vacuum layer—best overall performance;
- ✓ DGGTC with vacuum layer—excellent thermal performance, higher investment cost;
- ✓ SGGTC with air layer—simple design, lower thermal efficiency;
- ✓ DGGTC with air layer—high heat losses and embodied energy.

The results indicate that the choice of method (SAW or TOPSIS) does not significantly affect the decision outcome in this case. However, the introduction of TOPSIS strengthens the methodological foundation of the analysis and demonstrates the consistency of the model used.

4.7. Economic and Environmental Assessment Assumptions

The economic and environmental analyses were performed using material-related indicators derived from literature sources and representative engineering data. The calculations were based on the geometric characteristics of the collector components presented in Table 6 and the material properties summarized in Section 2.

The environmental assessment considered embodied energy and greenhouse gas emissions associated with the production of aluminium and glass, which constitute the principal materials used in the investigated collector configurations. Embodied energy and emission factors were adopted from previously published Life Cycle Assessment (LCA) studies related to solar thermal technologies and construction materials [17–24].

The economic analysis was based on material-related manufacturing costs of aluminium and glass. Representative market values were used to estimate production costs, while maintaining identical economic assumptions for all collector variants. This approach allows a direct comparison of the influence of collector design and structural complexity on overall economic performance.

The same input assumptions were applied consistently to all analysed configurations. Therefore, differences in the resulting economic and environmental indicators originate exclusively from variations in collector geometry, material consumption, and insulation strategy.

Table 10 summarizes the principal assumptions adopted in the economic and environmental assessment.

Table 10. Main assumptions used in the economic and environmental calculations.

Parameter	Value	Unit	Reference
Aluminium density	2700	kg/m^3	[48]
Glass density	2200	kg/m^3	[49]
Embodied energy of aluminium	53	kWh/kg	[17–24]
Embodied energy of glass	25.8	kWh/kg	[17–24]
CO_2 emission factor of aluminium	10.5	kg CO_2-eq/kg	[17–24]
CO_2 emission factor of glass	1.3	kg CO_2-eq/kg	[17–24]
Aluminium manufacturing cost	25	€/kg	Industrial market data
Glass manufacturing cost	76	€/kg	Industrial market data

5. Simplified Material-Footprint Assessment

A simplified material-footprint assessment was conducted to compare the material-related environmental burdens of the four analysed GTC configurations. The assessment is based on the quantified material inventory of the absorber and glass components and includes embodied energy and material-related GWP indicators. It does not constitute a complete ISO 14040/14044-compliant cradle-to-grave life cycle assessment.

5.1. Goal and Scope

The goal of the assessment was to quantify the embodied energy (E_{emb}) and global warming potential (GWP) for each GTC variant. The scope includes all major components: absorber plate, glass tubes, and supporting structures. Operational emissions were considered negligible due to the passive nature of the systems.

5.2. Life Cycle Inventory (LCI)

Data on mass and embodied energy were obtained from Tables 1 and 3. Emission factors for GWP were adopted from literature averages:

- Aluminum: 10.5 kg CO_2-eq/kg, 155 MJ/kg;
- Glass: 1.3 kg CO_2-eq/kg, 15 MJ/kg;
- $SnAl_2O_3$ coating and adhesives: estimated as 5 kg CO_2-eq/kg.

Recyclability factors were estimated based on material content.

5.3. Results and Interpretation

Table 11 presents the comparative LCA indicators for each GTC type.

Table 11. Unified material inventory and environmental indicators used in the environmental and MCDM analyses.

Configuration	Mass [kg]	Total Embodied Energy [kWh]	Annualized Embodied Energy [kWh/year]	Embodied GWP [kg CO_2-eq]
SG + Air	2.96	97.04	4.85	10.84
SG + Vacuum	2.96	97.04	4.85	10.84
DG + Air	5.60	165.15	8.26	14.27
DG + Vacuum	5.60	165.15	8.26	14.2

The data show that the SG + Vacuum configuration offers the most balanced environmental profile, with lower embodied energy and GWP than DG variants, while still achieving excellent thermal insulation. Although DG systems provide superior thermal resistance, their increased mass and complexity result in higher environmental burdens. The LCA results support the decision-making outcomes from the MCDM methods. The SG + Vacuum collector is not only the thermally and economically favorable choice, but also the most sustainable in terms of embodied energy and greenhouse gas emissions. Future designs may benefit from hybridizing lightweight structures with high-performing insulation layers to further reduce environmental impacts.

To ensure consistency between the geometric, economic, environmental, and MCDM analyses, a single component-level material inventory was adopted throughout the revised manuscript. The inventory is derived directly from the collector geometry and material densities used in the analytical model. The aluminium absorber mass is 0.76 kg, the inner/single glass tube mass is 2.20 kg, and the additional outer glass tube used in the double-glazed configurations has a mass of 2.64 kg. Consequently, the total material masses are 2.96 kg for the SG configurations and 5.60 kg for the DG configurations.

The same component masses are used for the calculation of embodied energy and material-related GWP. Total embodied energy is calculated from component mass multiplied by the corresponding material-specific embodied-energy factor. An annualized embodied-energy indicator is additionally reported by dividing the total embodied energy by the assumed 20-year service life; this quantity is explicitly distinguished from total embodied energy.

Components for which no quantitative mass inventory is available, including seals, adhesives, selective coating, and auxiliary supporting elements, are excluded from the quantitative material-footprint assessment and are identified as a limitation of the simplified system boundary.

6. Results and Discussion

The following figure (Figure 11) shows the glass temperature t_{gl} and heat losses Q_{loss} depending on the SGGTC types (with AL or VL), for different temperatures t_{abs} andt_o.

https://doi.org/10.3390/en19194497

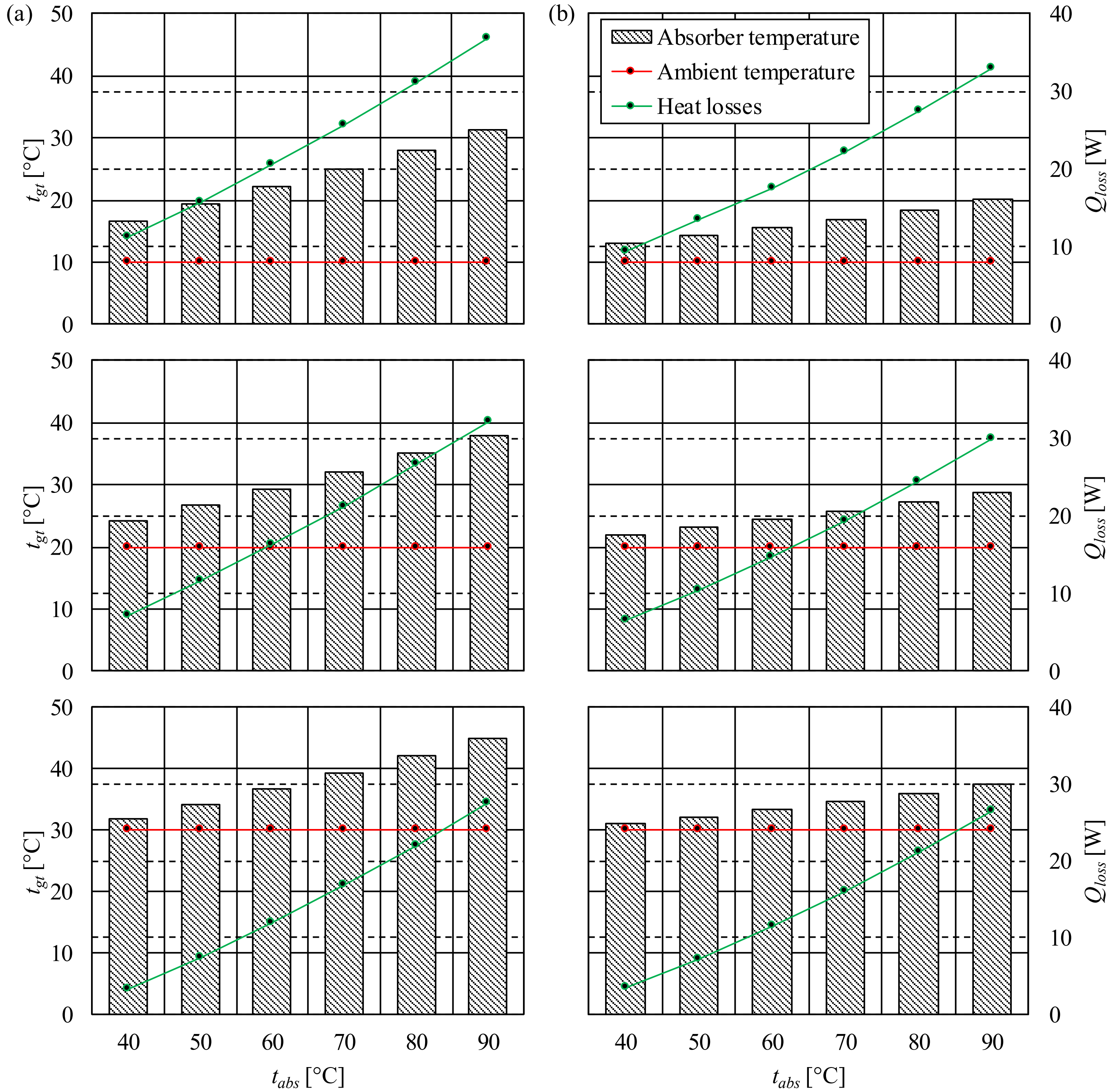

Figure 11. Characteristic temperatures and heat losses of the SGGTC with AL (**a**) or VL (**b**).

The red line in the diagrams represents t_o, the green line Q_{loss}, while the histograms indicate the change t_{gl}. On the abscissa axis for all analyzed cases, the displayed temperature t_{abs} is in the range 40–90 °C (step 10 °C). The values t_{gl} and Q_{loss} are also determined for different values t_o (10 °C, 20 °C, and 30 °C). All diagrams are presented on the same scale to see the differences between SGGTC with AL and SGGTC with VL.

The first thing that can be seen on the diagrams for SGGTC with AL (also valid for SGGTC with VL) is that the glass temperature t_{gl} increases with t_o increase, while on the other hand Q_{loss} decreases. It can also be concluded that growth t_{abs} brings it growth t_{gl} and Q_{loss}.

For the SGGTC with AL, heat losses increased monotonically with absorber temperature and decreased with increasing ambient temperature. Over the investigated operating range, Q_{loss} varied from 6.82 W to 73.58 W. Increasing the ambient temperature from 10 °C to 30 °C reduced heat losses by 25.18–69.49%, depending on the absorber temperature. The SGGTC with VL exhibited considerably lower heat losses, ranging from 3.46 W to 32.96 W. Under identical boundary conditions, vacuum insulation reduced heat losses by 49.32–57.44% compared with the air-filled configuration. The detailed temperature and heat-loss distributions are presented in Figure 11.

Analogous to the previous figure (Figure 11), the next figure (Figure 12) shows the temperatures $t_{gt,in}t_{gt,ext}$, and heat losses Q_{loss} depending on the DGGTC types (with AL or VL), for different temperatures t_{abs} and t_o.

In this case (Figure 12), two characteristic temperature histograms are presented (blue histograms for $t_{gt,in}$ and purple histograms fort$_{gt,ext}$).

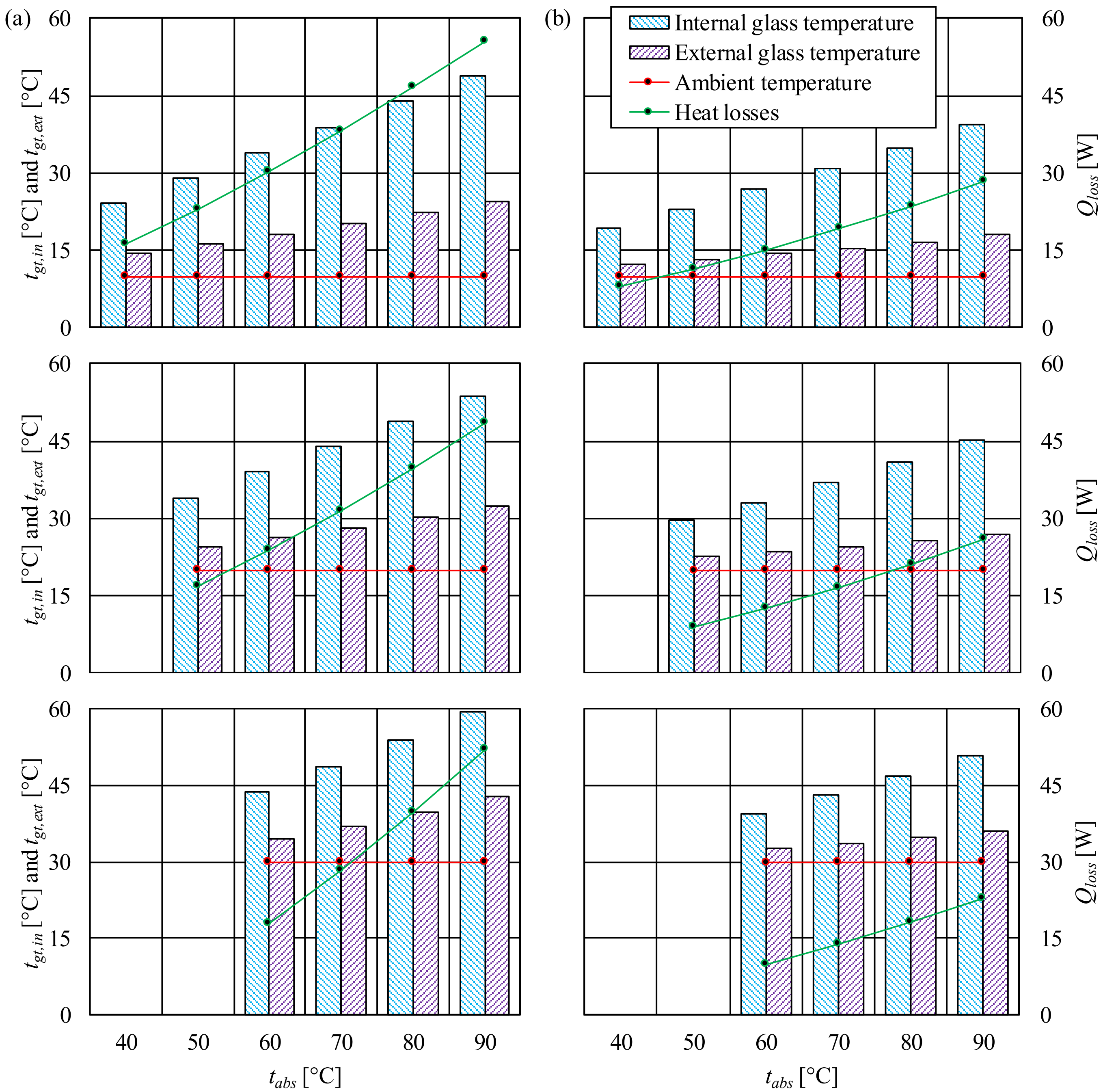

Figure 12. Characteristic temperatures and heat losses of the DGGTC with ALs (**a**) or VLs (**b**).

Figure 12 presents the characteristic inner- and outer-glass temperatures together with the corresponding heat losses for the double-glazed configurations. A similar thermal behaviour was observed for both DG configurations. For DG + Air, heat losses increased with absorber temperature and decreased with increasing ambient temperature, while the inner- and outer-glass temperatures followed the same general trends. The DG + Vacuum configuration consistently exhibited lower heat losses due to the suppression of convective heat transfer within both evacuated gaps. Under identical boundary conditions, vacuum insulation reduced heat losses by 44.92–55.91% relative to DG + Air.

These findings are consistent with experimental studies reported in the literature. Huang et al. [33] demonstrated that reducing heat transfer within an evacuated-tube collector by introducing heat shields increased thermal efficiency by up to 11.8% and reduced the loss-related coefficients of the instantaneous efficiency curve by 28.4% and 29.9%. Similarly, Zhang et al. [50] reported a 50.8% reduction in the overall heat-loss coefficient for a direct-flow evacuated-tube collector equipped with a heat shield. Although the collector geometries and thermal-loss suppression strategies differ from those considered in the present study, the reported improvements are of a similar order of magnitude and confirm the general trend that limiting convective and radiative heat transfer within the collector envelope substantially improves thermal insulation. The present reductions of 44.92–55.91% for DG + Vacuum and 49.32–57.44% for SG + Vacuum are therefore consistent with the thermal-performance improvements reported for related evacuated-tube collector systems.

In practical operation, the investigated GTC configurations are not expected to reach identical absorber temperatures because the operating temperature also depends on parameters such as the working-fluid mass flow rate and inlet water temperature. Therefore, representative operating temperatures were selected based on the present calculations and recommendations reported in [50,51]. Table 12 summarizes these representative absorber and glass temperatures together with the corresponding heat-loss values used in the subsequent MCDM analysis.

Table 12. Common reference operating conditions and recalculated heat-loss indicators used for the comparative MCDM analysis.

Configuration	t_{abs} [°C]	t_{amb} [°C]	w [m/s]	β [°]	Q_{loss} [W]	U_L [W/(m²K)]
SG + Air	60	20	1.0	40	32.87	8.22
SG + Vacuum	60	20	1.0	40	14.76	3.69
DG + Air	60	20	1.0	40	24.26	6.07
DG + Vacuum	60	20	1.0	40	12.69	3.17

The absolute results (from Table 6) of the different GTCs (SGGTC with AL, SGGTC with VL, DGGTC with AL, and DGGTC with VL) that can contribute to SAW, following different indicators in Figure 8, are presented in Table 8. Specific summary results are presented in Table 13.

Table 13. Summary results of the GTCs and criteria definition for the SAW analysis.

GTC	Space	$Q_{loss,avg}$ [W]	m [kg]	SO [m²]	TSO [m²]	VO [m³]	CM [€]	CE [€]	E_{emb} [kWh]	e_{CO2} [kg]
SGGTC	AL	15.66	2.96	0.11	0.35	0.0095	101	50.5	4.85	1058.65
	VL	11.73					111.1	55.55		792.97
DGGTC	AL	34.4	5.6	0.128	0.4	0.013	192	96	8.25	2325.51
	VL	24.43					220.8	110.4		1651.52

Based on the representative operating conditions summarized in Table 12, the MCDM procedure was carried out using geometric, economic, and ecological criteria. The adopted weighting scheme assigned 14% to geometric criteria, 50% to economic criteria, and 36% to ecological criteria. Within this framework, the SAW analysis indicated that the SG + Vacuum configuration achieved the best overall performance, followed by DG + Vacuum, SG + Air, and DG + Air. The same ranking order was confirmed by the TOPSIS method (Table 14).

The results showed that simpler constructions (in this case the SGGTC with VL), according to the main geometric, economic, and ecological criteria, are sometimes better solutions for their future user (Table 14). Heat losses in SCs represent an unused part of the energy that is returned to nature. More advanced solar constructions are characterized by higher thermal (useful) power, but this does not always mean that their heat losses will be lower and the thermal efficiency higher. With the increase in thermal power in many solar constructions, heat losses also increase, i.e., the amount of unused energy. If, for a change, heat losses were given priority, it would be concluded that solar technology is still not at its peak. In other words, there is still a lot of room for improvement.

Table 14. Final ranking of GTCs using the SAW and TOPSIS analysis.

GTC	SGGTC		DGGTC	
Specific indicator	AL	VL	AL	VL
S_i [-]	0.26318	0.19883	0.31577	0.22222
SAW Rank	3	1	4	2
S_i [-]	0.1875	0.8248	0.0839	0.7956
TOPSIS Rank	3	1	4	2

Vacuum technology additionally raises embodied energy investments, and thus also production investment costs. In this chain reaction, maintenance costs also increase. However, on the other hand, heat losses are then significantly reduced by 25.1% (SGGTC) and 28.98% (DGGTC), which proves that only a comprehensive approach can provide the possibility of correct selection of SC.

The consistency of rankings reinforces confidence in the methodological approach and suggests that the choice of MCDM technique (SAW or TOPSIS) does not significantly influence the final decision.

To further validate the stability of the ranking results, the TOPSIS method was employed as an alternative to SAW. TOPSIS provided a ranking identical to that of SAW, confirming the internal consistency of the multi-criteria evaluation. This redundancy in decision logic strengthens the credibility of the selected optimal collector design (SGGTC with vacuum layer) and supports its technical and environmental viability.

7. Conclusions

The main novel findings of this study can be summarized as follows:

Vacuum insulation provided the dominant thermal-performance improvement. Under identical boundary conditions, heat losses were reduced by 49.32–57.44% for SG + Vacuum relative to SG + Air and by 44.92–55.91% for DG + Vacuum relative to DG + Air. These results demonstrate that suppressing convection within the glass envelope provides a substantially greater thermal benefit than increasing structural complexity alone.

For the SG + Air configuration, the developed ETN model showed good agreement with published experimental data, with an estimated MAPE of 2.96% and a maximum relative error of approximately 5.63%. Quantitative validation was performed only for the

SG + Air configuration, supporting the applicability of the model to steady-state heat-loss prediction under the investigated conditions.

Both SAW and TOPSIS independently identified SG + Vacuum as the optimal configuration, followed by DG + Vacuum, SG + Air, and DG + Air. The identical ranking obtained with both methods demonstrates that the preferred configuration remains stable when different MCDM approaches are applied.

SG + Vacuum also provided the most favourable balance between thermal performance and material-related environmental impacts. Within the simplified material-footprint assessment, both single-glazed configurations had a total embodied energy of 97.04 kWh and an embodied GWP of 10.84 kg CO_2-eq, whereas both double-glazed configurations had corresponding values of 165.15 kWh and 14.27 kg CO_2-eq. Thus, the single-glazed configurations exhibited approximately 41.2% lower embodied energy and 24.0% lower embodied GWP than the double-glazed configurations. These findings indicate that the thermally best-performing solution does not require the structurally most complex collector design. One limitation of the proposed framework is its restriction to steady-state operating conditions. Future work should therefore extend the ETN approach to transient operating conditions and experimentally assess long-term vacuum degradation.

Author Contributions: Conceptualization, R.K. and A.N.; methodology, R.K. and A.N.; software, R.K., A.N., and P.L.; validation, A.N. and P.L.; formal analysis, R.K., A.N., and P.L.; investigation, R.K. and A.N.; resources, A.N.; data curation, A.N. and P.L.; writing—original draft, R.K., A.N., and P.L.; writing—review and editing, R.K.; visualization, A.N. and P.L.; supervision, R.K.; project administration, R.K. All authors have read and agreed to the published version of the manuscript.

Funding: This research received no external funding.

Data Availability Statement: The data presented in this study are available on request from the corresponding author.

Conflicts of Interest: The authors declare no conflicts of interest.

Nomenclature

Nomenclature:

A	Area, [m^2]
CE	Exploitation costs, [€]
CM	Manufacturing costs, [€]
cp	Specific heat, [J/(kg·K)]
D	Diameter, [m]
E	Energy, [kWh]
e	CO_2 emission, [kg]
g	Gravitational acceleration, [m/s^2]
h	Heat transfer coefficient, [W/(m^{2}K)]
K	Primary energy transformation coefficient, [-]
k	Thermal conductivity, [W/(m·K)]
L	Length, [m]
m	Mass, [kg]
Nu	Nusselt number, [-]
O	Circumference, [m]
Pr	Prandtl number, [-]
Q	Heat flux, [W]
R	Thermal resistance, [K/W]
Ra	Rayleigh number, [-]
Si	SAW score, [-]
SO	Surface occupation, [m^2]

T	Absolute temperature, [K]
time	Working time, [h]
TSO	Total surface occupation, [m^2]
V	Net volume, [m^3]
VO	Volume occupation, [m^3]
W	Wind speed, [m/s]
wj	Weight of j criterion performance, [%]
xij	Normalized value of i in terms of j criterion, [-]
Greek letters:	
β	Inclination angle, [rad]
δ	Thickness, [m]
ε	Emissivity, [-]
η	Efficiency, [-]
ν	Kinematic viscosity, [m^2/s]
ϱ	Density, [kg/m^3]
σ	Stefan-Boltzmann constant, [W/(m^{2}K^4)]
Subscripts:	
a	Air layer
abs	Flat absorber plate with an integrated circular cross-section flow channel
avg	Average
CO_2	Emission CO_2
con	Convection
e	Exterior dimension
el	Electricity
emb	Embodied
eq	Equivalent
ext	Exterior
gt	Glass tube
gtc	Glass tube collector
i	Interior dimension
in	Interior
loss	Heat loss
o	Ambient air
rad	Radiation
spec	Specific
tot	Total
VL	Vacuum layer
ǁ	Longitudinal plane
⊥	Transverse plane
Abbreviation:	
AA	Ambient air
ABS	Absorber
AL	Air layer
CPC	Compound parabolic concentrator
DG	Double-glazed
DGGTC	Double-glazed glass tube collector
EAL	Exterior air layer
EGT	Exterior glass tube
ETC	Evacuated tube collector
EVL	Exterior vacuum layer
FPC	Flat-plate collector
GT	Glass tube
GTC	Glass tube collector
IAL	Interior air layer
IC	Inner concentrating
IGT	Interior glass tube
IVL	Interior vacuum layer
MCA	Multi-criteria analysis

MCDM	Multi-criteria decision-making method
PV	Photovoltaic panel
PV-T	Photovoltaic-thermal collector
RES	Renewable energy source
SAW	Simple Additive Weighting
SC	Solar collector
SG	Single-glazed
SGGTC	Single-glazed glass tube collector

References

1. Kalogirou, S.A. Solar thermal collectors and applications. *Prog. Energy Combust. Sci.* **2004**, *30*, 231–295. https://doi.org/10.1016/j.pecs.2004.02.001.
2. Elahi, F.; Lotfi, M.; Shafiee, M. Comparative analysis of thermal and dynamic performance of glass evacuated tube solar collectors with U-pipe, filling pipe, and spiral pipe: An experimental study. *J. Therm. Anal. Calorim.* **2025**, *150*, 4359–4372. https://doi.org/10.1007/s10973-025-14045-7.
3. Nešović, A.; Lukić, N.; Kowalik, R.; Janaszek, A.; Taranović, D.; Kozłowski, T. Experimental and numerical comparison of glass tube collector with relative single-axis tracking and flat-plate collector without tracking during cloudy-sky days. *Sol. Energy* **2025**, *291*, 113412. https://doi.org/10.1016/j.solener.2025.113412.
4. Maia, C.B.; Ferreira, A.G.; Hanriot, S.M. Evaluation of a tracking flat-plate solar collector in Brazil. *Appl. Therm. Eng.* **2014**, *73*, 953–962.
5. Zhu, T.; Zhao, Y.; Diao, Y.; Li, F.-F.; Quan, Z. Experimental investigation and performance evaluation of a vacuum tube solar air collector based on micro heat pipe arrays. *J. Clean. Prod.* **2017**, *142*, 3517–3526. https://doi.org/10.1016/j.jclepro.2016.10.116.
6. Ahmadi, A.; Ehyaei, M.A.; Doustgani, A.; Assad, M.E.H.; Esmaeilion, F.; Hmida, A.; Jamali, D.H.; Kumar, R.; Li, Z.X.; Razmjoo, A. Recent progress in thermal and optical enhancement of low temperature solar collector. *Energy Syst.* **2023**, *14*, 1–40. https://doi.org/10.1007/s12667-021-00473-5.
7. Ramírez-Minguela, J.J.; Rangel-Hernández, V.H.; Alfaro-Ayala, J.A.; Elizalde-Blancas, F.; Ruiz-Camacho, B.; López-Núñez, O.A.; Alvarado-Rodríguez, C.E. Performance Comparison of Different Flat Plate Solar Collectors by Means of the Entropy Generation Rate Using Computational Fluid Dynamics. *Entropy* **2023**, *25*, 621. https://doi.org/10.3390/e25040621.
8. Zhang, D.; Diao, Y.; Wang, Z.; Pan, Y.; Sun, M.; Wang, X.; Du, P.; Zhao, Y. Thermal performance of two evacuated tube solar collectors with flat heat pipes. *Appl. Therm. Eng.* **2024**, *241*, 122366. https://doi.org/10.1016/j.applthermaleng.2024.122366.
9. Verma, S.K.; Gupta, N.K.; Rakshit, D. A comprehensive analysis on advances in application of solar collectors considering design, process and working fluid parameters for solar to thermal conversion. *Sol. Energy* **2020**, *208*, 1114–1150. https://doi.org/10.1016/j.solener.2020.08.042.
10. Mohamad, K. Exploring the influence of optical and thermal parameters on the effectiveness of parabolic trough collector receiver units. *Clean Energy* **2024**, *8*, 15–33. https://doi.org/10.1093/ce/zkae033.
11. Martínez-Manuel, L.; González-Canché, N.G.; López-Sosa, L.B.; Carrillo, J.G.; Wang, W.; Pineda-Arellano, C.A.; Cervantes, F.; Gil, J.J.A.; Peña-Cruz, M.I. A comprehensive analysis of the optical and thermal performance of solar absorber coatings under concentrated flux conditions. *Sol. Energy* **2022**, *239*, 319–336. https://doi.org/10.1016/j.solener.2022.05.015.
12. Caron, C.; Lauret, P.; Bastide, A. Machine Learning to speed up Computational Fluid Dynamics engineering simulations for built environments: A review. *Build. Environ.* **2025**, *267*, 112229. https://doi.org/10.1016/j.buildenv.2024.112229.
13. Hajabdollahi, Z.; Hajabdollahi, H. Thermo-economic modeling and multi-objective optimization of solar water heater using flat plate collectors. *Sol. Energy* **2017**, *155*, 191–202. https://doi.org/10.1016/j.solener.2017.06.023.
14. Liu, M.; Zhu, G.; Tian, Y. The historical evolution and research trends of life cycle assessment. *Green Carbon* **2024**, *2*, 425–437. https://doi.org/10.1016/j.greenca.2024.08.003.
15. Li, J.J.; Tian, Y.J.; Zhang, Y.L.; Xie, K.C. Assessing spatially multistage carbon transfer in the life cycle of energy with a novel multi-flow and multi-node model: A case of China's coal-to-electricity chain. *J. Clean. Prod.* **2022**, *339*, 130699.
16. Palazzo, J.; Geyer, R.; Suh, S. A review of methods for characterizing the environmental consequences of actions in life cycle assessment. *J. Ind. Ecol.* **2020**, *24*, 815–829.
17. Košičan, J.; Pardo Picazo, M.Á.; Vilčeková, S.; Košičanová, D. Life Cycle Assessment and Economic Energy Efficiency of a Solar Thermal Installation in a Family House. *Sustainability* **2021**, *13*, 2305. https://doi.org/10.3390/su13042305.
18. Madrigal, A.N.; Iyer-Raniga, U.; Yang, R.L. Exploring Design Thinking Processes in Circular Economy Strategies for PV Waste Management in Australia. *IOP Conf. Ser. Earth Environ. Sci.* **2024**, *1363*, 012051.

19. Thakur, S.; Singh, D.; Mughal, U.N.; Kumar, V.; Calay, R.K. Comparative Life Cycle Assessment of Solar Thermal, Solar PV, and Biogas Energy Systems: Insights from Case Studies. *Appl. Sci.* **2025**, *15*, 8082. https://doi.org/10.3390/app15148082.
20. Shrestha, N.; Zaman, A. Decommissioning and Recycling of End-of-Life Photovoltaic Solar Panels in Western Australia. *Sustainability* **2024**, *16*, 526.
21. Jachura, A.; Sekret, R. Life Cycle Assessment of the Use of Phase Change Material in an Evacuated Solar Tube Collector. *Energies* **2021**, *14*, 4146. https://doi.org/10.3390/en14144146.
22. Koroneos, C.; Nanaki, E.A. Life cycle environmental impact assessment of a solar water heater. *J. Clean. Prod.* **2012**, *37*, 154–161.
23. Souliotis, M.; Panaras, G.; Fokaides, P.A.; Papaefthimiou, S.; Kalogirou, S.A. Solar water heating for social housing: Energy analysis and Life Cycle Assessment. *Energy Build.* **2018**, *169*, 157–171. https://doi.org/10.1016/j.enbuild.2018.03.048.
24. Hemeida, M.G.; Hemeida, A.M.; Senjyu, T.; Osheba, D. Renewable Energy Resources Technologies and Life Cycle Assessment: Review. *Energies* **2022**, *15*, 9417. https://doi.org/10.3390/en15249417.
25. Taherdoost, H.; Madanchian, M. Multi-Criteria Decision Making (MCDM) Methods and Concepts. *Encyclopedia* **2023**, *3*, 77–87. https://doi.org/10.3390/encyclopedia3010006.
26. Sahoo, S.K.; Pamucar, D.; Goswami, S.S. A Review of Multi-Criteria Decision-Making Applications to Solve Energy Management Problems From 2010–2025: Current State and Future Research. *Spectr. Decis. Mak. Appl.* **2025**, *2*, 218–240. https://doi.org/10.31181/sdmap21202525.
27. Kumar, R.; Pamucar, D. A Comprehensive and Systematic Review of Multi-Criteria Decision-Making (MCDM) Methods to Solve Decision-Making Problems: Two Decades from 2004 to 2024. *Spectr. Decis. Mak. Appl.* **2025**, *2*, 177–196. https://doi.org/10.31181/sdmap21202524.
28. Rana, R.; Bhambri, P. Hybrid MCDM (Multi-Criteria Decision-Making) Approaches for Sustainable Energy Management. In *Modern SuperHyperSoft Computing Trends in Science and Technology*; IGI Global Scientific Publishing: Hershey, PA, USA, 2025; pp. 149–184.
29. Hosouli, S.; Hassani, R.A. Application of multi-criteria decision making (MCDM) model for solar plant location selection. *Results Eng.* **2024**, *24*, 103162. https://doi.org/10.1016/j.rineng.2024.103162.
30. Rezk, H.; Mukhametzyanov, I.Z.; Abdelkareem, M.A.; Salameh, T.; Sayed, E.T.; Maghrabie, H.M.; Radwan, A.; Wilberforce, T.; Elsaid, K.; Olabi, A.G. Multi-criteria decision making for different concentrated solar thermal power technologies. *Sustain. Energy Technol. Assess.* **2022**, *52*, 102118. https://doi.org/10.1016/j.seta.2022.102118.
31. *ISO 14040:2006*; Environmental Management—Life Cycle Assessment—Principles and Framework. International Organization for Standardization: Geneva, Switzerland, 2006.
32. *ISO 14044:2006*; Environmental Management—Life Cycle Assessment—Requirements and Guidelines. International Organization for Standardization: Geneva, Switzerland, 2006.
33. Huang, X.; Wang, Q.; Yang, H.; Zhong, S.; Jiao, D.; Zhang, K.; Li, M.; Pei, G. Theoretical and experimental studies of impacts of heat shields on heat pipe evacuated tube solar collector. *Renew. Energy* **2019**, *138*, 999–1009.
34. Rajput, R.K. *Engineering Thermodynamics: A Computer Approach*; Jones & Bartlett Publishers: Burlington, MA, USA, 2009.
35. Nešović, A.; Lukić, N.; Taranović, D.; Nikolić, N. Theoretical and experimental investigation of the glass tube solar collector with inclined NS axis and relative EW single-axis tracking flat absorber. *Appl. Therm. Eng.* **2024**, *236*, 121842.
36. Alsharari, M.; Armghan, A.; Aliqab, K. Parametric Optimization and Numerical Analysis of GaAs Inspired Highly Efficient I-Shaped Metamaterial Solar Absorber Design for Visible and Infrared Regions. *Appl. Sci.* **2023**, *13*, 2586. https://doi.org/10.3390/app13042586.
37. Kowalik, R. Artificial Intelligence in Photovoltaic-Integrated Buildings: From Energy Forecasting to Intelligent Control and Net-Zero Performance. *Energies* **2026**, *19*, 2534. https://doi.org/10.3390/en19112534.
38. Yan, B.; Wu, Q.; Chi, X.; Wu, C.; Luo, P.; Luo, Y.; Zeng, P. Numerical and Experimental Investigation of Photovoltaic/Thermal Systems: Parameter Analysis and Determination of Optimum Flow. *Sustainability* **2022**, *14*, 10156. https://doi.org/10.3390/su141610156.
39. Chauhan, R.; Singh, T.; Thakur, N.; Kumar, N.; Kumar, R.; Kumar, A. Heat transfer augmentation in solar thermal collectors using impinging air jets: A comprehensive review. *Renew. Sustain. Energy Rev.* **2018**, *82*, 3179–3190.
40. Hawwash, A.; Rahman, A.; Nada, S.; Ookawara, S. Numerical investigation and experimental verification of performance enhancement of flat plate solar collector using nanofluids. *Appl. Therm. Eng.* **2018**, *130*, 363–374.
41. Kim, H.; Ham, J.; Park, C.; Cho, H. Theoretical investigation of the efficiency of a U-tube solar collector using various nanofluids. *Energy* **2016**, *94*, 497–507.

42. Mitra, S.; Goswami, S.S. Application of simple average weighting optimization method in the selection of best desktop computer model. *Adv. J. Grad. Res.* **2019**, *6*, 60–68.
43. Tighnavard Balasbaneh, A.; Aldrovandi, S.; Sher, W. A Systematic Review of Implementing Multi-Criteria Decision-Making (MCDM) Approaches for the Circular Economy and Cost Assessment. *Sustainability* **2025**, *17*, 5007. https://doi.org/10.3390/su17115007.
44. Dean, M. Multi-criteria analysis. In *Advances in Transport Policy and Planning*; Academic Press: Cambridge, MA, USA, 2020; Volume 6, pp. 165–224.
45. Hammond, G.P.; Jones, C.I. Embodied energy and carbon in construction materials. *Proc. Inst. Civ. Eng. Energy* **2008**, *161*, 87–98. https://doi.org/10.1680/ener.2008.161.2.87.
46. Zabalza Bribián, I.; Valero Capilla, A.; Aranda Usón, A. Life cycle assessment of building materials: Comparative analysis of energy and environmental impacts and evaluation of the eco-efficiency improvement potential. *Build. Environ.* **2011**, *46*, 1133–1140. https://doi.org/10.1016/j.buildenv.2010.12.002.
47. Vasov, M.S.; Bogdanović, V.B.; Nedeljković, M.S.; Stanković, D.B.; Kostić, D.S.; Bogdanović-Protić, I.S. Reduction of CO_2 emission as a benefit of energy efficiency improvement: Kindergartens in the City of Niš—Case study. *Therm. Sci.* **2018**, *22*, 651–662. https://doi.org/10.2298/TSCI170704225V.
48. EnergyPlus Software. Available online: https://energyplus.net (accessed on 20 January 2024).
49. Clear Quartz Glass Plate. Available online: https://srla.shengbangdaquartz.com/quartz-glass-plate/clear-quartz-glass-plate.html (accessed on 12 April 2024).
50. Zhang, X.; You, S.; Ge, H.; Gao, Y.; Xu, W.; Wang, M.; He, T.; Zheng, X. Thermal performance of direct-flow coaxial evacuated-tube solar collectors with and without a heat shield. *Energy Convers. Manag.* **2014**, *84*, 80–87. https://doi.org/10.1016/j.enconman.2014.04.014.
51. Kowalik, R. Adaptive and Stepwise Solar Tracking Systems in Flat-Plate and Tubular Collectors: A Comprehensive Review of Thermal Performance, Modeling, and Techno-Economic Perspectives. *Energies* **2025**, *18*, 6106. https://doi.org/10.3390/en18236106.